Weakly Flux-Tunable Superconducting Qubit

José M. Chávez-Garcia,[1,*] Firat Solgun,[1] Jared B. Hertzberg,[1] Oblesh Jinka,[1] Markus Brink,[1] and Baleegh Abdo[1,†]

[1] *IBM Quantum, IBM Research Center, Yorktown Heights, New York 10598, USA.*

(Dated: March 9, 2022)

Flux-tunable qubits are a useful resource for superconducting quantum processors. They can be used to perform cPhase gates, facilitate fast reset protocols, avoid qubit-frequency collisions in large processors, and enable certain fast readout schemes. However, flux-tunable qubits suffer from a trade-off between their tunability range and sensitivity to flux noise. Optimizing this trade-off is particularly important for enabling fast, high-fidelity, all-microwave cross-resonance gates in large, high-coherence processors. This is mainly because cross-resonance gates set stringent conditions on the frequency landscape of neighboring qubits, which are difficult to satisfy with non-tunable transmons due to their relatively large fabrication imprecision. To solve this problem, we realize a coherent, flux-tunable, transmon-like qubit, which exhibits a frequency tunability range as small as 43 MHz, and whose frequency, anharmonicity and tunability range are set by a few experimentally achievable design parameters. Such a weakly tunable qubit is useful for avoiding frequency collisions in a large lattice while limiting its susceptibility to flux noise.

arXiv:2203.04164v1 [quant-ph] 8 Mar 2022

I. INTRODUCTION

Quantum computers promise significant speedup, over their classical counterparts, for certain hard computational problems, such as factoring and quantum chemistry [1–3]. However, for quantum computers to achieve a clear advantage over classical computers they need to run error correction codes and have sufficient quantum volumes [4]. One leading architecture for realizing such universal quantum computers is a crystal-like lattice of Josephson-junction-based qubits that supports the surface code or similar variations [5, 6]. But to realize such a generic architecture, it is critical to employ high-coherence qubits that are simple to fabricate and characterize, and high-fidelity two-qubit gates that are fast, easy to tune up, and, preferably, require a minimal hardware overhead. Two leading candidates that have been shown to satisfy these requirements are single Josephson-junction (JJ) transmons [7–9] and cross-resonance gates, which are fully controlled by microwave signals [10, 11]. In particular, single-JJ tansmons, formed by capacitively shunting a JJ (see Fig. 1(a)), exhibit coherence times on the order of a few hundreds of microseconds [12], and cross-resonance gates, which realize cNOT gates by generating a ZX-like interaction between two coupled qubits, regularly yield fidelities in excess of 99.1% with gate times of about 300 ns [13].

However, despite these favorable properties and numerous successful realizations of small quantum processors consisting of tens of single-JJ transmons and cross-resonance gates, deploying such qubits and gates in large quantum processors can be quite challenging. This is because cross-resonance gates, which are based on driving the control qubit at the target qubit frequency, set stringent lower and upper bounds on the first and second energy-level detunings of not only the control and target qubits but also their direct neighbors [14–18]. Satisfying these lower and upper bounds, which are necessary to avoid frequency collisions and slow gates, respectively, is particularly difficult to accomplish with single JJ-transmons. The difficulty arises from the fact that their fixed frequencies f_q are primarily determined by the JJ energies, which owing to uncontrolled parameters in the fabrication process, have random scatter with a standard deviation σ_f that is comparable to the upper bounds of the required detunings (set by the qubit anharmonicity). Such imprecision in the occurring transmon frequencies significantly increases the likelihood of frequency collisions between neighboring qubits and decreases the yield of collision-free chips. For example, a 'heavy hexagon' type lattice of qubits in a three-frequency pattern was shown to most effectively evade frequency-collisions [14]. Yet even the smallest-sized such lattice, containing 23 qubits, if fabricated with conventional precision of $\sigma_f/f_q \sim 3\%$, will be collision-free only 0.1% of the time [14].

To address this crippling frequency-collision problem in medium and large quantum processors, several strategies are being pursued, including: 1) replacing the single JJ-transmons with symmetric/asymmetric dc-SQUID transmons (see Fig. 1(b),(c)), whose frequency is tunable with external flux [7, 19]; 2) combining single-JJ transmons with large-anharmonicity qubits, such as capacitively-shunted flux qubits [20]; and 3) selectively modifying undesired transmon frequencies following fabrication and testing by etching a portion of their capacitive pads [21] or illuminating their JJs with focused laser beams for short durations [14, 15]. The first strategy enables precise qubit frequency tuning and the second eases frequency crowding, but in either case the qubits will suffer dephasing when tuned away from their flux-insensitive 'sweet spots.' The third strategy requires complex processing that is challenging to apply to large 3D-integrated and

*J.M.C-G, F.S., B.A. contributed equally to this work.
J.M.C-G current address: Center for Quantum Devices, Niels Bohr Institute, University of Copenhagen, 2100 Copenhagen, Denmark.
†Electronic address: babdo@us.ibm.com

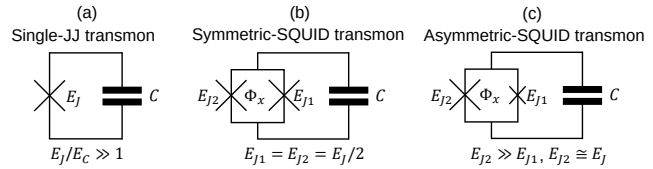


FIG. 1: Transmon circuits. (a) Fixed-frequency transmon consisting of a single Josephson junction with energy E_J shunted by a capacitor C. (b) Widely tunable transmon consisting of a symmetric dc-SQUID with identical junctions $E_{J1} = E_{J2} = E_J/2$ shunted by a capacitor C. The qubit frequency can be tuned using an external magnetic flux Φ_x threading the SQUID loop. (c) Medium-range tunable transmon consisting of an asymmetric dc-SQUID with dissimilar junctions $E_{J2} \gg E_{J1}$, where $E_{J2} \cong E_J$, shunted by a capacitor C.

packaged processors. The best demonstrated precision of such schemes is $\sigma_f = 14$ MHz, which can yield a collision-free 23-qubit device 70% of the time, but enables only 8% yield of a 127-qubit device and $\ll 0.1\%$ yield at 1000 qubit scale [14].

Here, we realize a superconducting qubit, named weakly tunable qubit (WTQ), that retains the desirable properties of single-JJ transmons in multi-qubit architectures and whose frequency tunes weakly with applied magnetic flux. Such a limited tunability could solve the frequency-collision problem in multi-qubit architectures while maintaining high coherence. This tunability could also improve qubit relaxation times by evading two-level systems (TLSs) in frequency space. According to Ref. [22], shifting a qubit by about 10 MHz can decouple it from the TLS and restore the qubit's T_1. Moreover, such a qubit could be beneficial in realizing high-fidelity parametric gates that rely on frequency modulation [23, 24].

Prior to introducing the WTQ circuit, we briefly highlight the drawbacks of existing tunable transmons, namely, the symmetric dc-SQUID transmon and the asymmetric dc-SQUID transmon, whose circuits are shown in Fig. 1 (b),(c). Since the frequency tunability range in the symmetric case can be large exceeding a gigahertz, its flux-noise sensitivity, which, to first order, increases with $|\mathrm{d}f_\mathrm{q}/\mathrm{d}\Phi_x|$, results in a significant dephasing away from the sweet spot [19]. In the asymmetric case on the other hand, a smaller tunability and sensitivity to flux noise can be achieved with large JJ-area ratio. But even with a ratio as high as 15 to 1, the smallest achievable tunability is about 330 MHz, which is much larger than what is needed to avoid frequency collisions. Furthermore, since the Josephson energy of the large-size JJ in the asymmetric SQUID (i.e., E_{J2}) is comparable to that of the single-JJ transmon (i.e., E_J), a significantly thicker oxide is required in the fabrication process to yield $E_{J2} \gg E_{J1}$ (see Fig. 1(c)). Such a thick oxide requirement increases the probability of lossy two-level systems in the JJs, potentially limiting the qubit lifetime.

The outline of the remainder of the paper is as follows. In Sec. II, we introduce the WTQ circuit. In Sec. III, we derive the WTQ Hamiltonian. In Sec. IV, we present analytical formulas for the frequency and anharmonicity of the WTQ and calculated response of a WTQ example. In Sec. V. we calculate the relaxation and dephasing rates of WTQs. In Sec. VI, we present experimental results, i.e., spectroscopy and coherence, taken of two 7-qubit chips that incorporate 6 WTQs and a fixed-frequency transmon each. In Sec. VII, we discuss the measurement results, offer additional theoretical predictions, and outline possible enhancements and future directions. Finally, in Sec. VIII, we provide a brief summary and highlight the advantages of employing WTQs in large quantum processors.

II. THE WTQ CIRCUIT

The WTQ circuit consists of three Josephson junctions J_1, J_2, J_3 with self-capacitances C_{J_1}, C_{J_2}, C_{J_3}, respectively, and three capacitors C_1, C_2 and C_c as shown in Fig. (2). The junctions J_2 and J_3 form a SQUID loop which is connected in series with the junction J_1. The junction J_1 shunted by the capacitance C_1 provides the main transmon mode of the qubit. The SQUID shunted by the capacitance C_2 generates a second transmon-type mode whose frequency is tuned by the external flux bias Φ_x threading the SQUID loop. Asymmetry is introduced in the SQUID by making the areas of the junctions J_2 and J_3 unequal to reduce the sensitivity to the flux noise [19]. The tunability of the qubit mode is achieved by the electrostatic interaction of the junction J_1 with the SQUID through the capacitance C_c.

In general, the underlying physics of WTQs is very similar to that of tunable coupling qubits (TCQs) [25–28], which also consist of two capacitively coupled transmons. TCQs and WTQs, however, differ in their circuit and functionality. While TCQs employ nominally identical symmetric SQUID transmons, WTQs employ a single-JJ and asymmetric SQUID transmons. TCQs also allow to independently tune their frequency and coupling strength to the readout resonator, whereas WTQs mainly enable their frequency to be tuned within a small range.

III. DERIVATION OF THE WTQ HAMILTONIAN

We will apply the circuit quantization formalism developed in [29] to derive the Hamiltonian of the WTQ circuit and will employ the analysis technique described in [30] to make a Born-Oppenheimer approximation and calculate the decoherence rates. To better describe the coupling of the WTQ to the flux bias circuitry we introduce a more detailed circuit model of the flux bias mechanism as shown in Fig. (3). The flux bias in the SQUID loop is generated by the DC current source I_B with impedance

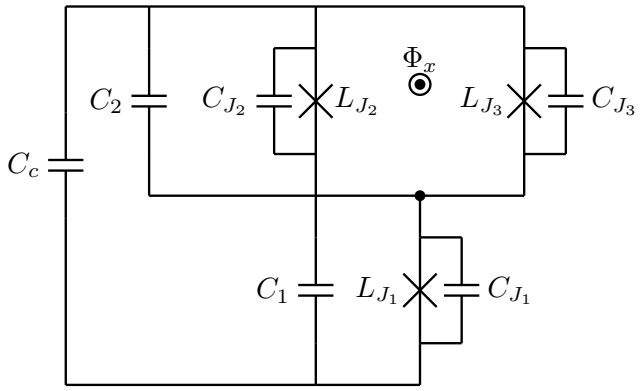


FIG. 2: Circuit diagram of the WTQ. It consists of three Josephson junctions with inductances L_{J_1}, L_{J_2}, L_{J_3} and self-capacitances C_{J_1}, C_{J_2}, C_{J_3}, respectively. The critical currents of the junctions are related to their inductances by the relation $I_{c,i} = \frac{\Phi_0}{2\pi L_{J_i}}$, for $i = 1, 2, 3$. The SQUID loop formed by the junctions J_2 and J_3 is biased by the external DC flux Φ_x. The sensitivity of the SQUID loop to the flux noise is reduced by making the areas of the junctions J_2 and J_3 unequal, i.e. $I_{c,3} = \alpha_J I_{c,2}$ for some $\alpha_J > 1$. Capacitors C_1 and C_2 shunting the junctions create the two main modes of the circuit: the qubit mode formed by J_1 shunted with C_1 and the high-frequency mode formed by C_2 shunting the SQUID loop. The electrostatic interaction of the qubit mode with the SQUID through the capacitance C_c provides the tunability of the WTQ.

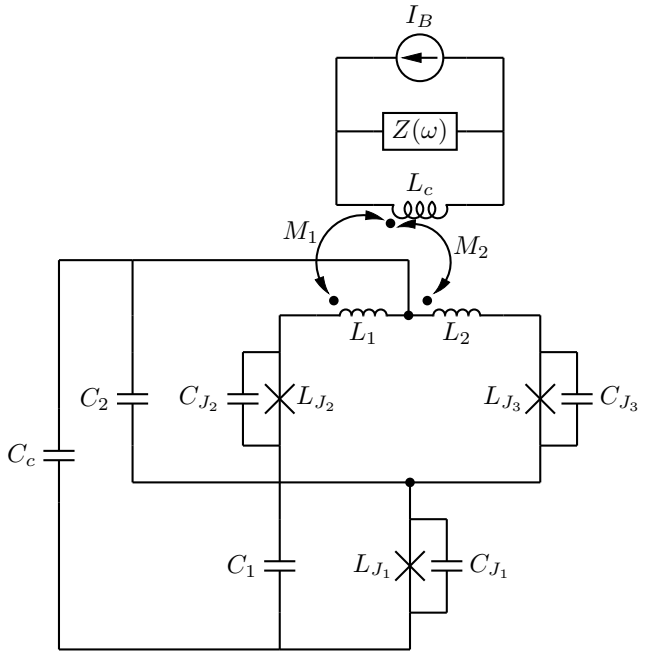


FIG. 3: Detailed WTQ Circuit Diagram. The flux bias in the SQUID loop is generated by the DC current source I_B with impedance $Z(\omega)$. L_c is the inductance of the coil that produces the magnetic field threading the SQUID loop. Two partial inductances [31] L_1 and L_2 are introduced to model the linear inductance of the SQUID loop which are inductively coupled to the coil with mutual inductances M_1 and M_2, respectively. Such a finely detailed construction of the WTQ circuit avoids inconsistenties in the calculation of the decoherence rates

$Z(\omega)$. Note that this construction is quite general in the sense that a wide range of circuits can be represented with this simple model by the Norton's theorem. The flux is coupled to the SQUID loop by a coil of inductance L_c. We have introduced two partial inductances L_1 and L_2 [31] to model the linear inductance of the SQUID loop which are coupled to the bias coil with mutual inductances M_1 and M_2. The finely detailed circuit model in Fig. (3) that carefully models the inductive network of the WTQ circuit and the flux bias circuitry is crucial for avoiding ambiguities in the calculation of the decoherence rates [32, 33]. Our Born-Oppenheimer treatment of the inductive network of the WTQ circuit, which reduces the capacitance matrix to unity, finds the irrotational gauge discussed in [32] that removes the inconsistencies associated with a gauge freedom.

Before applying the formalism in [29] we transform the capacitive network in the original WTQ circuit in Fig. (3) with the help of the multiport Belevitch transformer $\mathbf{T}$ as shown in Fig. (4). This transformation reduces the number of capacitors by one and help us bring the circuit to a form treatable in the formalism of [29] by making the capacitance matrix of the circuit diagonal:

$$\mathbf{C}_0 = \begin{pmatrix} C_A & 0 & 0 & 0 \\ 0 & C_{J_2} & 0 & 0 \\ 0 & 0 & C_{J_3} & 0 \\ 0 & 0 & 0 & C_B \end{pmatrix}, \tag{1}$$

where $C_A = C_1 + C_{J_1} + \frac{C_c C_2}{C_2 + C_c}$ and $C_B = C_2 + C_c$.

Also, since the number of degrees of freedom is given by the number of capacitors in the minimum spanning tree of the circuit, we reduce the number of degrees of freedom by one. The Belevitch transformer turns-ratio matrix $\mathbf{T}$ is given by

$$\mathbf{T} = \begin{pmatrix} t_{11} & t_{12} \\ t_{21} & t_{22} \end{pmatrix} = \begin{pmatrix} 1 & \frac{C_c}{C_2 + C_c} \\ 0 & 1 \end{pmatrix}, \tag{2}$$

which is obtained by a Cholesky Decomposition of the 2x2 impedance matrix defined looking into the purely capacitive network consisting of the capacitances C_1, C_2 and C_c.

The fundamental loop matrix defined in [29] is given by:

$$\mathbf{F}_{CL} = \begin{pmatrix} -t_{12} & t_{12} \\ 1 & 0 \\ 0 & -1 \\ -t_{22} & t_{22} \end{pmatrix} = \begin{pmatrix} -\frac{C_c}{C_2 + C_c} & \frac{C_c}{C_2 + C_c} \\ 1 & 0 \\ 0 & -1 \\ -1 & 1 \end{pmatrix}. \tag{3}$$

Note that the fundamental loop matrix of [29] is generalized to have real entries (turns ratios) other than 0,

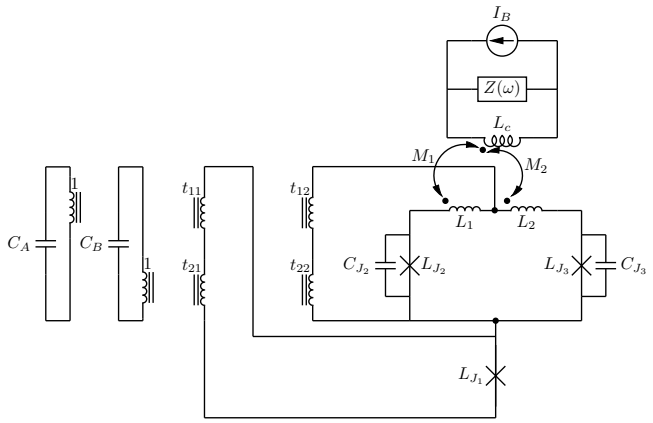


FIG. 4: Multiport Belevitch transformer with a turns-ratio matrix $\mathbf{T}$ is introduced to reduce the number of capacitors by one. The capacitance values are $C_A = C_1 + C_{J_1} + \frac{C_c C_2}{C_2+C_c}$ and $C_B = C_2 + C_c$. The turns-ratios are $t_{11} = 1$, $t_{12} = \frac{C_c}{C_2+C_c}$, $t_{21} = 0$ and $t_{22} = 1$. Note that C_{J_1} is added with C_1 and contributes to the value of the capacitance C_A.

1, and -1 [34].

We use Eq. (62) of [29] to calculate the inverse inductance matrix $\mathbf{M}_0$ as

$$\mathbf{M}_0 = \mathbf{F}_{CL}\tilde{\mathbf{L}}_L^{-1}\bar{\mathbf{L}}\mathbf{L}_{LL}^{-1}\mathbf{F}_{CL}^T. \tag{4}$$

To be able to calculate $\mathbf{M}_0$ we need to first introduce some auxiliary matrices related to the inductive network in the circuit that are defined in [29]. The inductance matrix $\mathbf{L}_t$ is defined in Eq. (1) of [29] as

$$\mathbf{L}_t = \begin{pmatrix} \mathbf{L} & \mathbf{L}_{LK} \\ \mathbf{L}_{LK}^T & \mathbf{L}_K \end{pmatrix} \tag{5}$$

$$= \begin{pmatrix} L_1 & 0 & M_1 \\ 0 & L_2 & M_2 \\ M_1 & M_2 & L_c \end{pmatrix}. \tag{6}$$

The inductance matrix $\mathbf{L}_t$ defined above is partitioned according to the choice of the tree and chord inductors in the network and the subscripts L and K denote chord and tree inductors, respectively. Hence L_1 and L_2 are chord inductors, whereas L_c is a tree inductor. Eqs. (32) and (33) of [29] define the matrices $\bar{\mathbf{L}}$ and $\bar{\mathbf{L}}_K$ as

$$\bar{\mathbf{L}} = \mathbf{L} - \mathbf{L}_{LK}\mathbf{L}_K^{-1}\mathbf{L}_{LK}^T \tag{7}$$

$$= \begin{pmatrix} L_1 - \frac{M_1^2}{L_c} & -\frac{M_1 M_2}{L_c} \\ -\frac{M_1 M_2}{L_c} & L_2 - \frac{M_2^2}{L_c} \end{pmatrix}, \tag{8}$$

$$\bar{\mathbf{L}}_K = \mathbf{L}_K - \mathbf{L}_{LK}^T\mathbf{L}^{-1}\mathbf{L}_{LK} \tag{9}$$

$$= L_c(1 - k_1^2 - k_2^2), \tag{10}$$

where we defined the inductive coupling coefficients k_1 and k_2 as $k_1 = \frac{M_1}{\sqrt{L_c L_1}}$ and $k_2 = \frac{M_2}{\sqrt{L_c L_2}}$. $\bar{\mathbf{L}}_K$ turns out to be a scalar since we have only L_c as a tree inductor in our circuit.

Next, we borrow some more definitions from [29] that are used in the definition of $\mathbf{M}_0$ in Eq. (4) above. Eq. (42) of [29] reads

$$\bar{\mathbf{F}}_{KL} = \mathbf{F}_{KL} - \mathbf{L}_K^{-1}\mathbf{L}_{LK}^T \tag{11}$$

$$= -\frac{1}{L_c}\begin{pmatrix} M_1 & M_2 \end{pmatrix}, \tag{12}$$

where we used the fact that $\mathbf{F}_{KL} = \begin{pmatrix} 0 & 0 \end{pmatrix}$ since the only tree inductor L_c does not belong to any of the fundamental loops defined by the chord inductors L_1 and L_2. Eq. (41) of [29] defines another auxiliary inductance matrix $\tilde{\mathbf{L}}_K$ as

$$\tilde{\mathbf{L}}_K = (\mathbf{1}_K - \mathbf{L}_K\bar{\mathbf{F}}_{KL}\mathbf{L}^{-1}\mathbf{L}_{LK}\bar{\mathbf{L}}_K^{-1})^{-1}\mathbf{L}_K \tag{13}$$

$$= L_c(1 - k_1^2 - k_2^2) \tag{14}$$

Again, similar to $\bar{\mathbf{L}}_K$ calculated above $\tilde{\mathbf{L}}_K$ turns out to be a scalar since we have only L_c as a tree inductor in the circuit. Next, we calculate two more matrices that appear in the definition of $\mathbf{M}_0$ in Eq. (4) above. Eq. (51) of [29] defines the matrix $\mathbf{L}_{LL}$ as

$$\mathbf{L}_{LL} = \bar{\mathbf{L}} + \mathbf{F}_{KL}^T\tilde{\mathbf{L}}_K\bar{\mathbf{F}}_{KL} \tag{15}$$

$$= \bar{\mathbf{L}}, \tag{16}$$

since $\mathbf{F}_{KL} = \begin{pmatrix} 0 & 0 \end{pmatrix}$ as we noted above. Eq. (47) of [29] defines the matrix $\tilde{\mathbf{L}}_L$ as

$$\tilde{\mathbf{L}}_L^{-1} = (\mathbf{1}_L + \mathbf{L}^{-1}\mathbf{L}_{LK}\bar{\mathbf{L}}_K^{-1}\tilde{\mathbf{L}}_K\bar{\mathbf{F}}_{KL})\bar{\mathbf{L}}^{-1} \tag{17}$$

$$= \begin{pmatrix} 1/L_1 & 0 \\ 0 & 1/L_2 \end{pmatrix}. \tag{18}$$

Using the definitions above we can now evaluate the expression for $\mathbf{M}_0$ given in Eq. (4) as

$$\mathbf{M}_0 = \mathbf{F}_{CL}\begin{pmatrix} 1/L_1 & 0 \\ 0 & 1/L_2 \end{pmatrix}\mathbf{F}_{CL}^T \tag{19}$$

$$= \begin{pmatrix} t_{12}^2\left(\frac{1}{L_1}+\frac{1}{L_2}\right) & -\frac{t_{12}}{L_1} & -\frac{t_{12}}{L_2} & t_{12}\left(\frac{1}{L_1}+\frac{1}{L_2}\right) \\ -\frac{t_{12}}{L_1} & \frac{1}{L_1} & 0 & -\frac{1}{L_1} \\ -\frac{t_{12}}{L_2} & 0 & \frac{1}{L_2} & -\frac{1}{L_2} \\ t_{12}\left(\frac{1}{L_1}+\frac{1}{L_2}\right) & -\frac{1}{L_1} & -\frac{1}{L_2} & \frac{1}{L_1}+\frac{1}{L_2} \end{pmatrix}. \tag{20}$$

The coupling vector $\mathbf{S}_0$ to the current source I_B is calculated using Eq. (66) of [29] as

$$\mathbf{S}_0 = \mathbf{F}_{CB} - \mathbf{F}_{CL}(\mathbf{L}_{LL}^{-1})^T\bar{\mathbf{F}}_{KL}^T\tilde{\mathbf{L}}_K^T\mathbf{F}_{KB} \tag{21}$$

$$= \begin{pmatrix} t_{12}\left((1-k_2^2)\frac{M_1}{L_1} - (1-k_1^2)\frac{M_2}{L_2} + k_1k_2\frac{(M_2-M_1)}{\sqrt{L_1L_2}}\right) \\ -(1-k_2^2)\frac{M_1}{L_1} - k_1k_2\frac{M_2}{\sqrt{L_1L_2}} \\ -(1-k_1^2)\frac{M_2}{L_2} + k_1k_2\frac{M_1}{\sqrt{L_1L_2}} \\ (1-k_2^2)\frac{M_1}{L_1} - (1-k_1^2)\frac{M_2}{L_2} + k_1k_2\frac{(M_2-M_1)}{\sqrt{L_1L_2}} \end{pmatrix} \tag{22}$$

$$\cong \begin{pmatrix} t_{12}\left(\frac{M_1}{L_1} - \frac{M_2}{L_2} + \frac{(M_2-M_1)}{\sqrt{L_1L_2}}\right) \\ -\frac{M_1}{L_1} - \frac{M_2}{\sqrt{L_1L_2}} \\ -\frac{M_2}{L_2} + \frac{M_1}{\sqrt{L_1L_2}} \\ \frac{M_1}{L_1} - \frac{M_2}{L_2} + \frac{(M_2-M_1)}{\sqrt{L_1L_2}} \end{pmatrix}, \tag{23}$$

using the auxiliary matrices introduced above and noting that $\mathbf{F}_{CB} = 0$ since none of the capacitors in the WTQ circuit belongs to the fundamental loop defined by the chord branch corresponding to the DC current source I_B and $\mathbf{F}_{KB} = -1$. In the last line above we used the fact that the inductive coupling constants k_1, k_2 are small; i.e. $k_1, k_2 \ll 1$ to simplify the expressions. We note here that the coupling vector $\bar{\mathbf{m}}_0$ (defined in Eq. (65) of [29]) to the impedance $Z(\omega)$ is given by

$$\bar{\mathbf{m}}_0 = \mathbf{F}_{CZ} - \mathbf{F}_{CL}(\mathbf{L}_{LL}^{-1})^T\bar{\mathbf{F}}_{KL}^T\tilde{\mathbf{L}}_K^T\mathbf{F}_{KZ} \tag{24}$$

$$= -\mathbf{S}_0, \tag{25}$$

since $\mathbf{F}_{CZ} = 0$ and $\mathbf{F}_{KZ} = 1$. We will use $\bar{\mathbf{m}}_0$ in later sections to calculate the decoherence rates of the WTQ.

Hence, we can write the Hamiltonian of the WTQ circuit in the initial frame as

$$\mathcal{H} = \frac{1}{2}\mathbf{Q}^T\mathbf{C}_0^{-1}\mathbf{Q} + \frac{1}{2}\mathbf{\Phi}^T\mathbf{M}_0\mathbf{\Phi} + \mathbf{\Phi}^T\mathbf{S}_0 I_B - \sum_{i=1}^{3} E_{J_i}\cos(\varphi_{J_i}), \tag{26}$$

where $\mathbf{\Phi} = \frac{\Phi_0}{2\pi}(\varphi_{J_1}, \varphi_{J_2}, \varphi_{J_3}, \varphi_4)$. Here, the first three coordinates are the phases across the junctions whereas the last coordinate φ_4 is the phase across the capacitor C_B. $\mathbf{Q}$ is the vector of charge variables canonically conjugate to the fluxes $\mathbf{\Phi}$.

To find the DC flux bias developed across each junction in the limit of small loop inductances $L_1 \to 0$, $L_2 \to 0$ and to determine the coupling of the WTQ to the impedance $Z(\omega)$ we need to perform a few coordinate transformations:

$$\mathbf{R}_0 = \begin{pmatrix} 1 & 0 & 0 & 0 \\ t_{12} & 1 & 0 & 1 \\ t_{12} & 0 & 1 & 1 \\ 0 & 0 & 0 & 1 \end{pmatrix} \tag{27}$$

$$\mathbf{R}_1 = \begin{pmatrix} 1 & 0 & 0 & 0 \\ 0 & 1 & 0 & 0 \\ 0 & 0 & 1 & 0 \\ -t_{12}\frac{(C_{J_2}+C_{J_3})}{C_b} & -\frac{C_{J_2}}{C_b} & -\frac{C_{J_3}}{C_b} & 1 \end{pmatrix}, \tag{28}$$

$$\mathbf{R}_2 = \begin{pmatrix} 1 & -\frac{C_{J_2}C_c}{C_aC_b} & -\frac{C_{J_3}C_c}{C_aC_b} & 0 \\ 0 & 1 & 0 & 0 \\ 0 & 0 & 1 & 0 \\ 0 & 0 & 0 & 1 \end{pmatrix}, \tag{29}$$

where we defined

$$C_a = C_1' + \frac{C_2'C_c}{C_2' + C_c}, \tag{30}$$

$$C_b = C_2 + C_c + C_{J_2} + C_{J_3}, \tag{31}$$

with $C_1' = C_1 + C_{J_1}$ and $C_2' = C_2 + C_{J_2} + C_{J_3}$. Next we do a capacitance re-scaling as required by the Born-Oppenheimer treatment of [30]

$$\mathbf{A} = \begin{pmatrix} \sqrt{C_a} & 0 & 0 & 0 \\ 0 & \sqrt{C_{11}} & -\beta\sqrt{C_{22}} & 0 \\ 0 & 0 & \sqrt{C_{22}} & 0 \\ 0 & 0 & 0 & \sqrt{C_b} \end{pmatrix} \tag{32}$$

with

$$C_{11} = C_{J_2}\frac{C_{\alpha,3}C_{\beta,3}}{C_aC_b}, \tag{33}$$

$$C_{22} = C_{J_3}\frac{C_AC_B}{C_{\alpha,3}C_{\beta,3}}, \tag{34}$$

$$\beta = \sqrt{\frac{C_{J_2}C_{J_3}}{C_aC_b}}\frac{(C_1' + C_c)}{\sqrt{C_AC_B}}, \tag{35}$$

and

$$C_{\alpha,3} = C_1' + \frac{C_c\,(C_2 + C_{J_3})}{C_2 + C_c + C_{J_3}}, \tag{36}$$

$$C_{\beta,3} = C_2 + C_c + C_{J_3}. \tag{37}$$

All four coordinate transformations can be combined into one, i.e., $\mathbf{R}_t$, such that

$$\mathbf{R}_t = \mathbf{R}_0\mathbf{R}_1\mathbf{R}_2\mathbf{A}^{-1}. \tag{38}$$

The initial capacitance matrix $\mathbf{C}_0$ is transformed into the identity matrix by the total transformation $\mathbf{R}_t$ as

$$\mathbf{C}_0 \to \mathbf{R}_t^T\mathbf{C}_0\mathbf{R}_t = \mathbf{1}. \tag{39}$$

This ensures the choice of the irrotational gauge that removes the inconsistencies in the decoherence rate calculations as discussed in [32].

Initial flux coordinate vector $\mathbf{\Phi}$ is transformed into the final capacitance re-scaled coordinate vector $\mathbf{f}$ by

$$\mathbf{\Phi} = \mathbf{R}_t \mathbf{f}. \tag{40}$$

Phases across the junctions can be written in terms of the final coordinates $\mathbf{f} = (f_1, f_2, f_3, f_4)^T$ as

$$\varphi_{J_1} = \alpha_{11} f_1 + \alpha_{12} f_2 + \alpha_{13} f_3 + \alpha_{14} f_4, \tag{41}$$
$$\varphi_{J_2} = \alpha_{21} f_1 + \alpha_{22} f_2 + \alpha_{23} f_3 + \alpha_{24} f_4, \tag{42}$$
$$\varphi_{J_3} = \alpha_{31} f_1 + \alpha_{32} f_2 + \alpha_{33} f_3 + \alpha_{34} f_4, \tag{43}$$

with

$$\alpha_{11} = \frac{1}{\sqrt{C_a}}, \quad \alpha_{21} = \left(\frac{C_c}{C_b}\right)\frac{1}{\sqrt{C_a}}, \quad \alpha_{31} = \left(\frac{C_c}{C_b}\right)\frac{1}{\sqrt{C_a}}, \tag{44}$$

$$\alpha_{14} = 0, \quad \alpha_{24} = \frac{1}{\sqrt{C_b}}, \quad \alpha_{34} = \frac{1}{\sqrt{C_b}}, \tag{45}$$

$$\alpha_{12} = -\frac{C_c\sqrt{C_{J_2}}}{\sqrt{C_a C_b C_{\alpha,3} C_{\beta,3}}}, \quad \alpha_{13} = -\frac{C_c\sqrt{C_{J_3}}}{\sqrt{C_A C_B C_{\alpha,3} C_{\beta,3}}}, \tag{46}$$

$$\alpha_{22} = \frac{1}{\sqrt{C_{J_2}}}\sqrt{\frac{C_{\alpha,3} C_{\beta,3}}{C_a C_b}}, \quad \alpha_{23} = 0, \tag{47}$$

$$\alpha_{32} = -\frac{(C_1' + C_c)\sqrt{C_{J_2}}}{\sqrt{C_a C_b C_{\alpha,3} C_{\beta,3}}}, \quad \alpha_{33} = \frac{1}{\sqrt{C_{J_3}}}\sqrt{\frac{C_A C_B}{C_{\alpha,3} C_{\beta,3}}}. \tag{48}$$

Hence, we can write the system Hamiltonian in the capacitance re-scaled final coordinates $\mathbf{f}$ as

$$\mathcal{H} = \frac{1}{2}\mathbf{q}_f^T \mathbf{q}_f + U(\mathbf{f}), \tag{49}$$

where $\mathbf{q}_f$ is the vector of momenta canonically conjugate to the final coordinates $\mathbf{f}$ and the potential $U(\mathbf{f})$ is given by

$$U(\mathbf{f}) = \frac{1}{2}\mathbf{f}^T \mathbf{R}_t^T \mathbf{M}_0 \mathbf{R}_t \mathbf{f} + \mathbf{f}^T \mathbf{R}_t^T \mathbf{S}_0 I_B - \sum_{i=1}^{3} E_{J_i} \cos(\varphi_{J_i}). \tag{50}$$

Born-Oppenheimer Approximation

We perform the Born-Oppenheimer approximation following [30]. The coordinates f_2 and f_3 are fast coordinates denoted by the vector $\mathbf{f}_\perp = (f_2, f_3)$ and will be eliminated. Since the potential seen is very steep along the direction of the fast coordinates it can be approximated with a harmonic potential as given by the Eq. (14) in [30]

$$U(\mathbf{f}) \approx V(\mathbf{f}_\parallel) + \sum_i a_i (\mathbf{f}_\perp)_i + \sum_{i,j} b_{ij} (\mathbf{f}_\perp)_i (\mathbf{f}_\perp)_j, \tag{51}$$

where $\mathbf{f}_\parallel = (f_1, f_4)$ is the vector holding the slow coordinates and the matrix $\mathbf{b} = [b_{ij}]$ is the 2x2 sector (corresponding to the coordinates f_2 and f_3) of the transformed $\mathbf{M}_0$ matrix in the final frame; i.e. of the matrix $\mathbf{R}_t^T \mathbf{M}_0 \mathbf{R}_t$:

$$\mathbf{b} = \begin{pmatrix} \frac{1}{\alpha_{22}^2 C_{J_2}^2 L_1} & \frac{1}{C_{23} L_1} \\ \frac{1}{C_{23} L_1} & \frac{1}{\alpha_{33}^2 C_{J_3}^2 L_2} + \frac{(C_1' + C_c)^2 C_{J_3}}{C_A C_B C_{\alpha,3} C_{\beta,3} L_1} \end{pmatrix}, \tag{52}$$

where we defined $C_{23}^{-1} = \sqrt{\frac{C_{J_3} C_a C_b}{C_{J_2} C_A C_B}} \frac{(C_1' + C_c)}{C_{\alpha,3} C_{\beta,3} L_1}$. The vector $\mathbf{a} = (a_1, a_2)$ in Eq. (51) holds the entries (corresponding to the fast coordinates f_2 and f_3) of the transformed $\mathbf{S}_0$ vector in the final frame; i.e. of the vector $\mathbf{R}_t^T \mathbf{S}_0$ (with the scale factor I_B/φ_0):

$$\mathbf{a} = \begin{pmatrix} -\frac{M_1}{\alpha_{22} C_{J_2} L_1} \\ -\frac{(C_1' + C_c)\sqrt{C_{J_3}} M_1}{\sqrt{C_A C_B C_{\alpha,3} C_{\beta,3}} L_1} + \frac{M_2}{\alpha_{33} C_{J_3} L_2} \end{pmatrix} \left(\frac{I_B}{\varphi_0}\right), \tag{53}$$

where $\varphi_0 \equiv \Phi_0/2\pi$ is the reduced flux quantum.

The potential is centered around

$$\left(\mathbf{f}_\perp^{\min}\right)_0 = \begin{pmatrix} \alpha_{22} C_{J_2} \left(M_1 + \frac{(C_1' + C_c) C_{J_3}}{C_{\alpha,3} C_{\beta,3}} M_2 \right) \\ -\alpha_{33} C_{J_3} M_2 \end{pmatrix} \left(\frac{I_B}{\varphi_0}\right) \tag{54}$$

for the fast coordinates (here, we dropped terms quadratic in the small inductive coupling coefficients k_1, k_2). This is the DC component of the fast coordinates that does not depend on the slow coordinates. We used the Eq. (16) of [30] to calculate $\left(\mathbf{f}_\perp^{min}\right)_0$:

$$\left(\mathbf{f}_\perp^{\min}\right)_0 = -\frac{1}{2}\mathbf{b}^{-1}\mathbf{a}. \tag{55}$$

Hence, the reduced DC flux bias in the phases of the junctions is

$$\varphi_x^{(0)} = \begin{pmatrix} \varphi_{x,1}^{(0)} \\ \varphi_{x,2}^{(0)} \\ \varphi_{x,3}^{(0)} \end{pmatrix} = \begin{pmatrix} \alpha_{12} & \alpha_{13} \\ \alpha_{22} & \alpha_{23} \\ \alpha_{32} & \alpha_{33} \end{pmatrix} \left(\mathbf{f}_{\perp}^{min}\right)_0 \tag{56}$$

$$= \begin{pmatrix} \frac{C_c\left(C_{J_3}M_2 - C_{J_2}M_1\right)}{C_a C_b} \\ \frac{C_{\alpha,3}C_{\beta,3}}{C_a C_b}M_1 + \frac{\left(C_1'+C_c\right)C_{J_3}}{C_a C_b}M_2 \\ -\frac{\left(C_1'+C_c\right)C_{J_2}}{C_a C_b}M_1 - \frac{C_{\alpha,2}C_{\beta,2}}{C_a C_b}M_2 \end{pmatrix} \left(\frac{I_B}{\varphi_0}\right), \tag{57}$$

where we defined

$$C_{\alpha,2} = C_1' + \frac{C_c(C_2 + C_{J_2})}{C_2 + C_c + C_{J_2}}, \tag{58}$$

$$C_{\beta,2} = C_2 + C_c + C_{J_2}. \tag{59}$$

We note here that $\varphi_x = \varphi_{x,2}^{(0)} - \varphi_{x,3}^{(0)} = (M_1 + M_2)\left(\frac{I_B}{\varphi_0}\right)$, as expected.

We perform the Born-Oppenheimer approximation by expanding the cosine potentials around the DC flux biases in Eq. (54) for the fast coordinates to obtain the following effective Hamiltonian:

$$\mathcal{H} = \frac{1}{2}\mathbf{q}^T\mathcal{C}^{-1}\mathbf{q} - E_{J_1}\cos\left(\varphi_1 + \varphi_{x,1}^{(0)}\right) - E_2\cos\left(\varphi_2 + \varphi_x^{(2)}\right), \tag{60}$$

where

$$\mathcal{C} = \begin{pmatrix} C_1' + C_c & -C_c \\ -C_c & C_2' + C_c \end{pmatrix}, \tag{61}$$

$$E_2 = \left(E_{J_2} + E_{J_3}\right)\cos\left(\frac{\varphi_x}{2}\right)\sqrt{1 + d^2\tan^2\left(\frac{\varphi_x}{2}\right)}, \tag{62}$$

$$\varphi_x^{(2)} = \frac{\left(\varphi_{x,2}^{(0)} + \varphi_{x,3}^{(0)}\right)}{2} - \tan^{-1}\left(d\tan\left(\frac{\varphi_x}{2}\right)\right), \tag{63}$$

with $d = \left(E_{J_3} - E_{J_2}\right)/\left(E_{J_2} + E_{J_3}\right)$, $\varphi_1 = f_1/\sqrt{C_a}$, $\varphi_2 = f_2/\sqrt{C_b}$, $E_{J_1} = \varphi_0 I_{J1}$, $E_{J_2} = \varphi_0 I_{J2}$, and $E_{J_3} = \varphi_0 I_{J3}$.

Eq. (60) is the Hamiltonian corresponding to two transmon qubits with Josephson energies E_{J_1} and E_2 and shunting capacitances C_1' and C_2' coupled electrostatically with capacitance C_c.

IV. WTQ FREQUENCY AND ANHARMONICITY

At this point we can calculate the qubit frequency ω_q using formulas derived in [35]

$$\omega_q = \omega_1\sqrt{1 - \frac{r^2\omega_1^2}{\omega_2^2 - (1-r^2)\omega_1^2}}, \tag{64}$$

where ω_1 is the bare frequency of the qubit mode given by [35]

$$\omega_1 = \omega_{J_1} - \frac{E_{C_1}/\hbar}{1 - E_{C_1}/(\hbar\omega_{J_1})}, \tag{65}$$

with

$$E_{C_1} = \frac{e^2}{2\left(C_1' + C_c\right)}, \tag{66}$$

and

$$\omega_{J_1} = \frac{1}{\sqrt{L_{J_1}\left(C_1' + C_c\right)}}. \tag{67}$$

The coupling coefficient r in Eq. (64) between the modes of the WTQ is defined by

$$r = \frac{C_c}{\sqrt{C_1'C_2' + C_c\left(C_1' + C_2'\right)}}. \tag{68}$$

The charging energy E_{C_2} for the high-frequency SQUID mode is

$$E_{C_2} = \frac{e^2\left(1 + r^2\right)}{2\left(C_2' + C_c\right)}. \tag{69}$$

Bare frequency ω_2 of the SQUID mode is given by

$$\omega_2 = \omega_{J_2} - \frac{E_{C_2}/\hbar}{1 - E_{C_2}/\left(\hbar\omega_{J_2}\right)}, \tag{70}$$

with

$$\omega_{J_2} = \frac{1}{\sqrt{L_{J_S}\frac{\left(C_2'+C_c\right)}{(1+r^2)}}}, \tag{71}$$

where we defined the effective SQUID inductance L_{J_S}

$$L_{J_S} = \left(\left(\frac{1}{L_{J_2}} + \frac{1}{L_{J_3}}\right)\left|\cos\left(\frac{\varphi_x}{2}\right)\right|\sqrt{1 + d^2\tan^2\left(\frac{\varphi_x}{2}\right)}\right)^{-1}. \tag{72}$$

Anharmonicity α of the qubit mode can be estimated by [35]

$$\alpha = -E_{C_1}\left(\frac{\omega_{J_1}}{\omega_1}\right)^2\left(1 - \frac{r^2\omega_1^2}{\omega_2^2 - (1-r^2)\omega_1^2}\right)^3. \tag{73}$$

In Fig. 5(a),(b) we plot the transition frequency $f_{01} = f_q = \omega_q/2\pi$ and the anharmonicity α of a WTQ as a

function of the normalized applied flux. The device parameters in this example are chosen to yield a WTQ with $f_{01}^{\max}$ and α of about 5 GHz and 300 MHz, respectively, and frequency tunability $\delta = 50$ MHz. In the calculation, we use the analytical formulas of Eqs. (64) and (73), which we plot as red dashed curves and compare them to the results obtained using the exact diagonalization of the qubit Hamiltonian specified in Eq. (60) in the charge basis (Bloch-wave basis), which we plot as blue solid curves. As seen in Fig. 5(b), the WTQ anharmonicity varies with the applied flux. But the variation is relatively small of about 17 MHz in this example, between the minimum and maximum sweet spots (based on the exact calculation). Similarly, we plot in Fig. 5(c), using blue solid and red dashed curves, the exact and analytical solutions for the high-frequency mode of the qubit f_{10} versus the normalized applied flux. The slight bending in the exact diagonalization curve (the solid blue), seen around 14 GHz, is due to the crossing of f_{10}, the first excited level of the SQUID oscillator, and the third level of the qubit.

V. CALCULATION OF THE DECOHERENCE RATES

We will now employ Fermi Golden-Rule type formulas in Eqs. (10-11) of [30] to calculate the relaxation and dephasing rates of the WTQ:

$$\frac{1}{T_1} = \frac{4}{\hbar}\left|\langle 0|\,\bar{\mathbf{m}}^T\mathbf{f}\,|1\rangle\right|^2 J\left(\omega_{01}\right)\coth\left(\frac{\hbar\omega_{01}}{2k_BT}\right), \tag{74}$$

$$\frac{1}{T_\phi} = \frac{1}{\hbar}\left|\langle 0|\,\bar{\mathbf{m}}^T\mathbf{f}\,|0\rangle - \langle 1|\,\bar{\mathbf{m}}^T\mathbf{f}\,|1\rangle\right|^2 \left.\frac{J(\omega)}{\hbar\omega}\right|_{\omega\to 0} 2k_BT, \tag{75}$$

where $\bar{\mathbf{m}}$ is the vector giving the coupling to the impedance in the final frame, that is

$$\bar{\mathbf{m}} = \mathbf{R}_t^T\bar{\mathbf{m}}_{\mathbf{0}} = \begin{pmatrix} 0 \\ \frac{C_aC_bM_1}{\sqrt{C_{J_2}C_{\alpha,3}C_{\beta,3}L_1}} \\ \frac{(C_1'+C_c)\sqrt{C_{J_3}}M_1}{\sqrt{C_AC_BC_{\alpha,3}C_{\beta,3}L_1}} - \sqrt{\frac{C_{\alpha,3}C_{\beta,3}}{C_AC_BC_{J_3}}}\frac{M_2}{L_2} \\ 0 \end{pmatrix}. \tag{76}$$

Hence, we see that only the fast coordinates (f_2 and f_3) are coupled to the decoherence source which is the impedance $Z(\omega)$.

The spectral density $J(\omega)$ of the bath due to the impedance $Z(\omega)$ is calculated using Eq. (93) of [29] (up to the scale factors)

$$J(\omega) = \mathrm{Im}\left[K(\omega)\right] = \frac{\omega\mathrm{Re}\left[Z(\omega)\right]}{\omega^2L_c^2 + \left|Z\right|^2 + 2\omega L_c\mathrm{Im}\left[Z(\omega)\right]}, \tag{77}$$

where $K(\omega)$ is the kernel function of the bath given in Eq. (73) of [29] as

$$K(\omega) = \bar{\mathbf{L}}_Z^{-1}(\omega). \tag{78}$$

$\bar{\mathbf{L}}_Z$ is defined in Eq. (58) of [29] as

$$\bar{\mathbf{L}}_Z = \mathbf{L}_{ZZ} - \mathbf{L}_{ZL}\mathbf{L}_{LL}^{-1}\mathbf{L}_{LZ}, \tag{79}$$

where $\mathbf{L}_{ZZ}$ is given in Eq. (52) of [29] as

$$\mathbf{L}_{ZZ} = \mathbf{L}_Z + \mathbf{F}_{KZ}^T\tilde{\mathbf{L}}_K\mathbf{F}_{KZ} \tag{80}$$

$$= \mathbf{L}_Z + \tilde{\mathbf{L}}_K \tag{81}$$

$$= \frac{Z(\omega)}{i\omega} + L_c(1-k_1^2-k_2^2), \tag{82}$$

where in the second line above we used the fact that $\mathbf{F}_{KZ} = 1$ and in the third line we used Eq. (14). $\mathbf{L}_{ZL}$ is given by Eq. (53) of [29] as

$$\mathbf{L}_{ZL} = \mathbf{F}_{KL}^T\tilde{\mathbf{L}}_K\mathbf{F}_{KZ} = 0, \tag{83}$$

since $\mathbf{F}_{KL} = 0$. Hence, $\bar{\mathbf{L}}_Z$ in Eq. (79) above is given by

$$\bar{\mathbf{L}}_Z = \mathbf{L}_{ZZ} \tag{84}$$

$$= \frac{Z(\omega)}{i\omega} + L_c(1-k_1^2-k_2^2). \tag{85}$$

Now Eq. (78) for $K(\omega)$ reads

$$K(\omega) = \bar{\mathbf{L}}_Z^{-1}(\omega) \tag{86}$$

$$= \frac{i\omega}{Z(\omega) + i\omega L_c(1-k_1^2-k_2^2)}. \tag{87}$$

Furthermore, calculating $\mathrm{Im}\left[K(\omega)\right]$ using Eq. (87) yields the result of Eq. (77) since $k_1, k_2 \ll 1$.

The dependence of the argument $\bar{\mathbf{m}}^T\mathbf{f}$ of the matrix elements on the slow coordinates φ_1 and φ_2 can be calculated using Eqs. (16-20) of [30]. Eq. (16) of [30] reads

$$\left(\mathbf{f}_\perp^{min}\right)\left(\mathbf{f}_\parallel\right) = -\frac{1}{2}\mathbf{b}^{-1}\mathbf{a}(\mathbf{f}_\parallel), \tag{88}$$

where $\left(\mathbf{f}_\perp^{min}\right)\left(\mathbf{f}_\parallel\right)$ gives the dependence of the fast coordinates on the slow coordinates with

$$\mathbf{a}(\mathbf{f}_\parallel) = \begin{pmatrix} \alpha_{12} & \alpha_{22} & \alpha_{32} \\ \alpha_{13} & \alpha_{23} & \alpha_{33} \end{pmatrix}\begin{pmatrix} \sin\left(\varphi_{J_1}\right)/L_{J_1} \\ \sin\left(\varphi_{J_2}\right)/L_{J_2} \\ \sin\left(\varphi_{J_3}\right)/L_{J_3} \end{pmatrix}. \tag{89}$$

Hence,

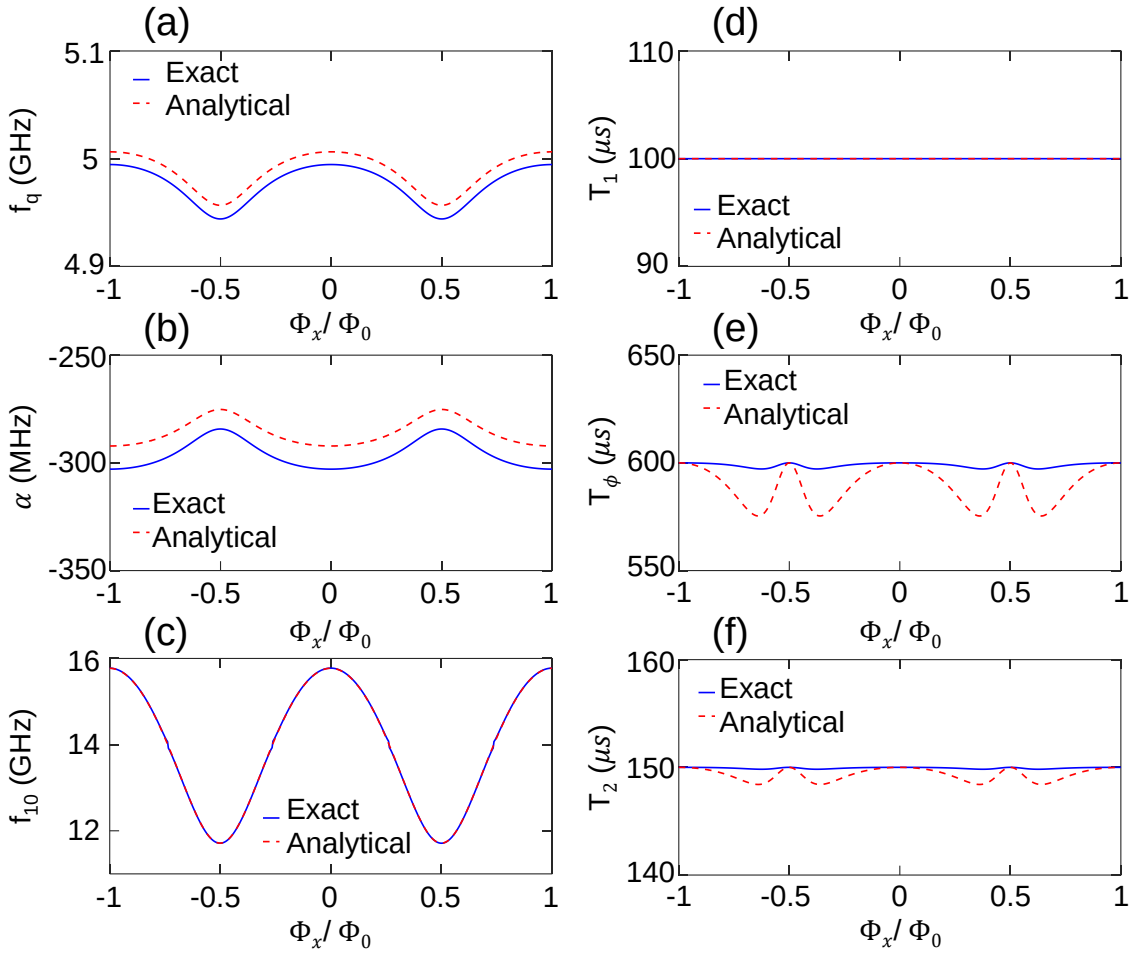


FIG. 5: A WTQ example. (a) Qubit frequency and (b) anharmonicity of the WTQ as a function of the normalized flux threading the SQUID loop. In this example, the WTQ has a maximum frequency and anharmonicity of about 5 GHz and 300 MHz, respectively and exhibit a frequency tunability $\delta = 50$ MHz. Blue curves are obtained by the diagonalization of the Hamiltonian in Eq. (60) in the charge basis. Red dashed curves are calculated using the analytical formulas in Eqs. (64) and (73). (c) The high-frequency mode of the WTQ f_{10} versus normalized flux. The WTQ circuit parameters employed in this example are $I_{c1} = I_{c2} = 26$ nA, $I_{c3} = \alpha_J I_{c2}$, $\alpha_J = 3.5$, $C_1' = 50$ fF, $C_2' = 20$ fF, $C_c = 20$ fF, where $C_{J_1} = C_{J_2} = 1$ fF and $C_{J_3} = \alpha_J C_{J_2}$. In plots (d), (e), (f), we evaluate the dependence of the WTQ coherence times, i.e., T_1, T_ϕ, and T_2 on the applied flux. In this calculation, we assume $T = 0.02$ K and $Z(\omega) = R = 0.1$ Ohm and that the maximum values for T_1 and $T_2 = 1.5T_1$, i.e., 100 μs and 150 μs respectively, are set by loss or noise sources that are independent of flux or the flux biasing circuit. The T_2 curves in (f) are calculated using the relation $1/T_2 = 1/2T_1 + 1/T_\phi$, which also sets the maximum for T_ϕ in (e). The analytical calculation of T_1 and T_ϕ uses the matrix element results of Eqs. (96-103). The exact calculation employs Eqs. (74), (75) with a diagonalization of the Hamiltonian in Eq. (60).

$$\bar{\mathbf{m}}^T \mathbf{f} = \bar{\mathbf{m}}_\perp^T \left(\mathbf{f}_\perp^{min}\right)\left(\mathbf{f}_\parallel\right) \tag{90}$$

$$= A_s^{(1)} \sin\left(\varphi_{J_1}\right) + A_s^{(2)} \sin\left(\varphi_{J_2}\right) + A_s^{(3)} \sin\left(\varphi_{J_3}\right), \tag{91}$$

where $\bar{\mathbf{m}}_\perp$ is the sub-vector of $\bar{\mathbf{m}}$ corresponding to the fast coordinates and

$$\mathbf{A}_s = \begin{pmatrix} A_s^{(1)} \\ A_s^{(2)} \\ A_s^{(3)} \end{pmatrix} = \begin{pmatrix} \frac{C_c\left(C_{J_2} M_1 - C_{J_3} M_2\right)}{C_a C_b L_{J_1}} \\ -\frac{C_{\alpha,3} C_{\beta,3} M_1 + (C_1' + C_c) C_{J_3} M_2}{C_a C_b L_{J_2}} \\ \frac{\left(C_1' + C_c\right) C_{J_2} M_1 + C_{\alpha,2} C_{\beta,2} M_2}{C_a C_b L_{J_3}} \end{pmatrix}. \tag{92}$$

Note that we dropped the DC flux bias terms in the expression in Eq. (90) above. The last two terms in the above expression can again be combined in a single sine function as:

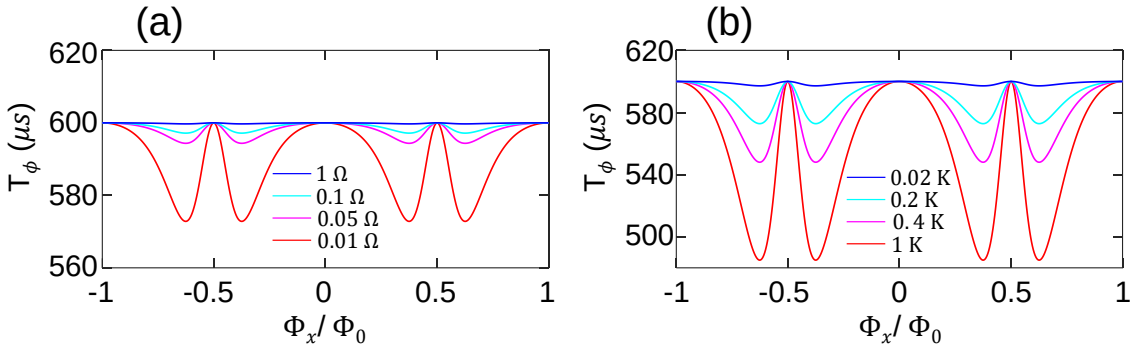


FIG. 6: Dependence of WTQ dephasing time T_ϕ on the normalized flux threading the SQUID loop for varying parameter R (a) and T (b) of the flux biasing circuit, where $Z(\omega) = R$ is assumed. In (a) and (b) the values of T and R are set to 0.02 K and 0.1 Ohm, respectively. The WTQ circuit parameters employed in this calculation are the same as Fig. 5. The curves in both plots are obtained by the diagonalization of the Hamiltonian in Eq. (60) in the charge basis along with Eqs. (74), (75).

$$\bar{\mathbf{m}}^T\mathbf{f} = A_s^{(1)}\sin\left(\varphi_1+\varphi_{x,1}^{(0)}\right) + A\cos\left(\frac{\varphi_x}{2}\right)\sqrt{1+d_s^2\tan^2\left(\frac{\varphi_x}{2}\right)}\sin\left(\varphi_2+\varphi_x^{(s)}\right), \tag{93}$$

where $A = A_s^{(2)} + A_s^{(3)}$, $d_s = \left(A_s^{(2)} - A_s^{(3)}\right)/\left(A_s^{(2)} + A_s^{(3)}\right)$ and $\varphi_x^{(s)} = \left(\varphi_{x,2}^{(0)} + \varphi_{x,3}^{(0)}\right)/2 + \tan^{-1}\left(d_s\tan\left(\varphi_x/2\right)\right)$.

Matrix elements can be evaluated by assuming harmonic wavefunctions for the main qubit mode and the SQUID mode. Since the coupling between the two modes is dispersive, we can write the excited level $\widetilde{|1\rangle}$ of the qubit as:

$$\widetilde{|1\rangle} \approx \left(1-\frac{\epsilon^2}{2}\right)|10\rangle - \epsilon\,|01\rangle\,, \tag{94}$$

where $\epsilon = \frac{J_{12}}{\Delta}$. Here the excitation on the left under the ket corresponds to the qubit mode, whereas the right excitation corresponds to the SQUID mode and $\Delta = \omega_2 - \omega_1$ is the detuning between the qubit and SQUID modes. The coupling rate J_{12} between the qubit and SQUID mode is given by

$$J_{12} = \frac{1}{2\sqrt{Z_1 Z_2}}\frac{C_c}{C_1'C_2' + C_c(C_1'+C_2')}, \tag{95}$$

where Z_1 is the characteristic impedance of the qubit mode and Z_2 is the characteristic impedance of the SQUID mode, which are given by

$$Z_1 = \frac{1}{\omega_1(C_1'+C_c)},$$
$$Z_2 = \sqrt{\frac{L_{J_S}}{(C_2'+C_c)\left(1-\frac{2E_{C_2}}{\hbar\omega_2}\right)}}.$$

Using symmetry arguments one can show that

$$\widetilde{\langle 0|}\sin\left(\varphi_1+\varphi_x^{(1)}\right)\widetilde{|0\rangle} = 0, \tag{96}$$
$$\widetilde{\langle 1|}\sin\left(\varphi_1+\varphi_x^{(1)}\right)\widetilde{|1\rangle} = 0. \tag{97}$$

Using Eq. (94), we get

$$\widetilde{\langle 1|}\sin\left(\varphi_2+\varphi_x^{(s)}\right)\widetilde{|1\rangle} = \left(1-\frac{\epsilon^2}{2}\right)^2\langle 10|\sin\left(\varphi_2+\varphi_x^{(s)}\right)|10\rangle + \epsilon^2\langle 01|\sin\left(\varphi_2+\varphi_x^{(s)}\right)|01\rangle\,. \tag{98}$$

Hence,

$$\begin{aligned}\langle 0|\,\bar{\mathbf{m}}^T\mathbf{f}\,|0\rangle - \langle 1|\,\bar{\mathbf{m}}^T\mathbf{f}\,|1\rangle &\approx \epsilon^2\langle 10|\sin\left(\varphi_2+\varphi_x^{(s)}\right)|10\rangle \\ &\quad - \epsilon^2\langle 01|\sin\left(\varphi_2+\varphi_x^{(s)}\right)|01\rangle \\ &= \epsilon^2\eta_2^2\exp\left(-\frac{\eta_2^2}{2}\right)\sin\left(\varphi_\Delta\right),\end{aligned} \tag{99}$$

where

$$\varphi_\Delta = \tan^{-1}\left(d\tan\left(\frac{\varphi_x}{2}\right)\right) + \tan^{-1}\left(d_s\tan\left(\frac{\varphi_x}{2}\right)\right), \tag{100}$$

$$\eta_2^2 = 4\pi \left(\frac{Z_2}{R_Q} \right), \tag{101}$$

and $R_Q = \frac{h}{e^2} \approx 25813\Omega$ is the resistance quantum.

The matrix elements in the T_1 expression in Eq. (74) can be calculated as:

$$\begin{aligned} \widetilde{\langle 0|} \sin\left(\varphi_1 + \varphi_x^{(1)}\right) \widetilde{|1\rangle} &= \langle 00| \sin\left(\varphi_1 + \varphi_x^{(1)}\right) |10\rangle \\ &= \eta_1 \exp\left(-\frac{\eta_1^2}{2}\right), \end{aligned} \tag{102}$$

with $\eta_1^2 = 4\pi \left(\frac{Z_1}{R_Q}\right)$ and

$$\begin{aligned} \widetilde{\langle 0|} \sin\left(\varphi_2 + \varphi_x^{(s)}\right) \widetilde{|1\rangle} &= \epsilon^2 \langle 00| \sin\left(\varphi_2 + \varphi_x^{(s)}\right) |01\rangle \\ &= \epsilon^2 \eta_2 \exp\left(-\frac{\eta_2^2}{2}\right) \cos\left(\varphi_\Delta\right). \end{aligned} \tag{103}$$

Using the WTQ example of Fig. 5(a)-(c), we compare in Figs. 5(d),(e) the calculation for the relaxation and pure dephasing times as a function of normalized applied flux based on Eqs. (74), (75) and the diagonalization of the Hamiltonian (Eq. (60)) versus the approximate results obtained using the analytical expressions for the matrix elements derived above, where in both cases we assume a constant, real impedance $Z(\omega) = R$. To complete the picture, we plot in Fig. 5(f) the expected decoherence time T_2 for the same WTQ example given by the relation $T_2^{-1} = (2T_1)^{-1} + T_\phi^{-1}$. In our theoretical evaluation of the coherence times of the qubit, i.e., T_1, T_ϕ, and T_2, we make the following assumptions, (1) the maximum relaxation time 100 μs of the qubit is limited by a loss mechanism that is unrelated to the flux biasing source, such as dielectric loss. (2) the maximum decoherence time of the qubit T_2 is equal to $1.5T_1$ and limited by a non-flux noise source, such as thermal photon population in the readout resonator, (3) the parameters R and T associated with the flux biasing circuit are 0.01 Ohm and 0.1 K, respectively.

Furthermore, to illustrate the dependence of the dephasing time on the parameter R of the flux-biasing circuit for fixed $T = 0.02$ K, we use the WTQ example of Fig. 5 and plot in Fig. 6(a) the exact solution of T_ϕ versus normalized applied flux corresponding to varying parameter R. The blue, cyan, magenta, and red curves in Fig. 6(a) correspond to $R = 1, 0.1, 0.05, 0.01$ Ohm, respectively. As expected, we find that the dips in T_ϕ away from the sweet spots increase with decreasing R. This is because the smaller the resistance in parallel with the current source is (see Fig. 3), the larger the current portion flowing through it.

Likewise, in Fig. 6(b), we illustrate the dependence of T_ϕ on the parameter T, while keeping $R = 0.1$ Ohm constant. The blue, cyan, magenta, and red curves in Fig. 6(b) correspond to $T = 0.02, 0.2, 0.4, 1$ K, respectively. As expected in this case as well, the dips in T_ϕ away from the sweet spots increase with T of the flux-biasing circuit resistor that is in parallel with the current source (see Fig. 3).

VI. EXPERIMENTAL RESULTS

We realize and measure two seven-qubit chips (referred to as A and B), which are similar in design to those with single JJ-transmons we measured in the past [17]. Each chip includes six WTQs and one single-JJ transmon as shown in the device photo in Fig. 7(a). Each qubit is capacitively coupled to a readout resonator, which, in turn, is capacitively coupled to a readout port. All resonator buses coupling the qubits are disabled by shortening their ends to ground. We implement the WTQs in two configurations, dubbed P-shape and U-shape, which differ in the shape of the gap-capacitance electrodes shunting the JJs. In the P-shape configuration exhibited in Fig. 7(b), the three capacitance electrodes are parallel to each other, whereas in the U-shape configuration displayed in Fig. 7(c), one of the outer electrodes wraps around three sides of the middle electrode of the qubit. The motivation for designing WTQs using these two possible configurations is to experimentally examine if either holds any coherence advantage over the other. In Fig. 7(d), we exhibit a simplified circuit of the WTQ. The shunting capacitances C_1', C_2' include the capacitances of the JJs. Figure 7d also outlines the useful parameter space of WTQ capacitances and Josephson energies (i.e., in comparison to the transmon qubits presented in Fig. 1).

In what follows, we present the main results measured for chip A and B, whose circuit parameters are listed in Tables I, II for chip A and Tables III, IV for chip B. The WTQs in chip A yield a smaller δ range $43-99$ MHz (see Table I) versus $115-288$ MHz (see Table III) for chip B, since they are designed with a slightly higher JJ area ratio of the SQUIDs, i.e., $\alpha_S = A_{J_3}/A_{J_2}$, where A_{J_2} and A_{J_3} represent the design area of the respective junctions. In chip A, we set $\alpha_S = 4.2$ for WTQ1, WTQ3, WTQ6, WTQ7, versus $\alpha_S = 2.9$ for the corresponding qubits in chip B, and $\alpha_S = 5.1$ for WTQ2 and WTQ5 in chip A versus $\alpha_S = 3.0$ in chip B. The two chips also differ in the JJ oxidation conditions applied in fabrication, yielding higher maximum WTQ frequencies for chip B, i.e., $5.5-5.97$ GHz, than chip A, i.e., $4.44-4.89$ GHz. Lastly, chips A and B are measured in two different cooldowns using different dc wiring between the 4 K stage and the base-temperature stage (20 mK) of the dilution fridge. In the case of chip A, the intermediate dc wiring is superconducting while in the case of chip B, it is resistive.

In Fig. 8(a)-(d), we show spectroscopy measurements of WTQ2 (P-shape), WTQ3 (P-shape), WTQ5 (U-shape), and WTQ6 (U-shape) of chip A, respectively,

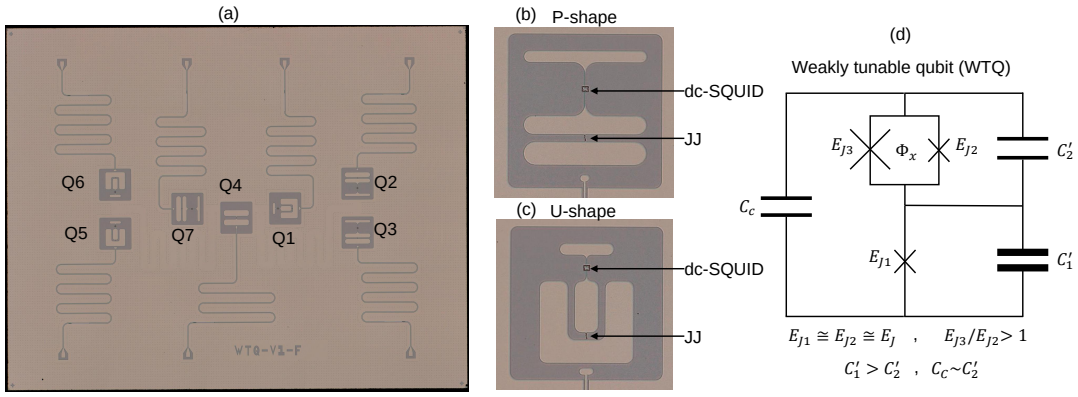


FIG. 7: (a) A photo of one of the two 7-qubit chips measured in this work. The chip consists of 6 WTQs and one single-JJ transmon (Q4). The WTQs are realized using two gap-capacitance geometries shown in (b) and (c). (b) P-shape WTQ (Q2, Q3, Q7), in which the capacitance pads are parallel. (c) U-shape WTQ (Q1, Q5, Q6), in which one capacitance pad is curved. (d) Equivalent WTQ circuit. C_1' and C_2' represent the total capacitance shunting the JJs (including the self capacitance of the JJs). The small junction of the SQUID is comparable to the junction of the single-JJ transmon $E_{J2} \cong E_{J1} \cong E_J$, whereas the other JJ of the SQUID is slightly larger, giving $\alpha_J = 2 - 5$. Rounded corners used in the electrodes are an effort to minimize E field concentration and are not specific to the WTQ design.

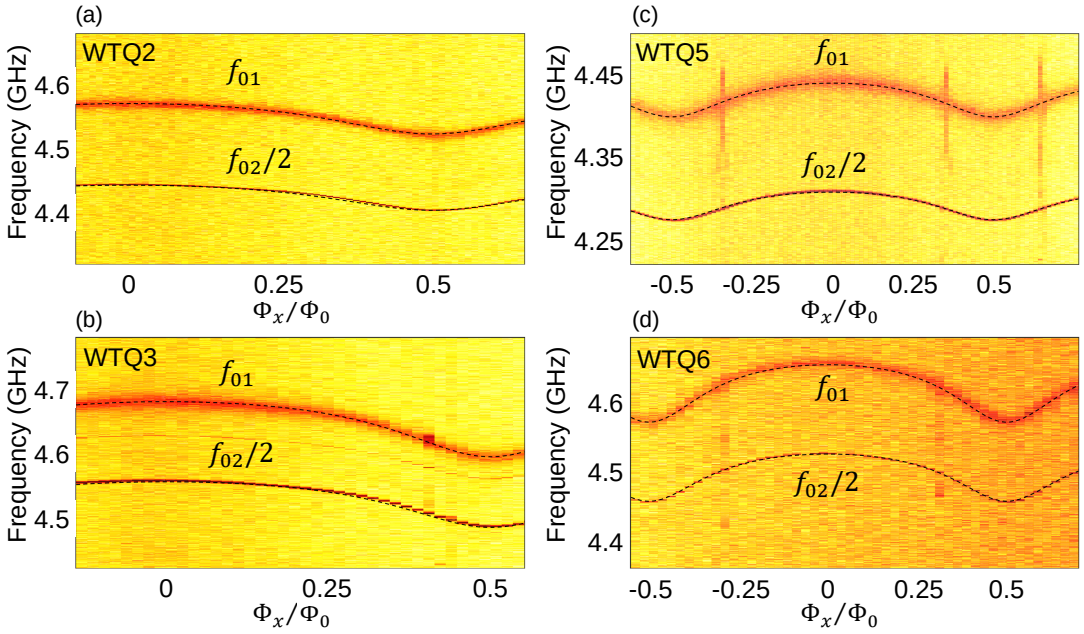


FIG. 8: Representative qubit spectroscopy measurements of chip A plotted versus normalized external flux. The data shows f_{01}, and $f_{02}/2$ curves. (a) WTQ2 (P-shape). (b) WTQ3 (P-shape). (c) WTQ5 (U-shape). (d) WTQ6 (U-shape). WTQ2 and WTQ5, having $\alpha_J = 3.5$, exhibit a small tunability of 50 MHz and 43 MHz, respectively. WTQ3 and WTQ6, having $\alpha_J = 2.8$, exhibit a slightly larger tunability of 89 MHz and 86 MHz. Dashed black curves are theory fits.

plotted versus the normalized external flux threading the SQUID loop. The magnetic flux is generated using a dc-current I_B applied to a small global superconducting coil with $L_c \backsimeq 5.5$ mH attached to the device copper package. The mutual inductance M between the coil and the SQUID loops across the chip vary in the range $0.8 - 1.1$ pH. The dashed black curves plotted over the data represent theoretical fits for the qubit frequency f_{01} and $f_{02}/2$. In Table II, we list the capacitance and critical current parameters of the various qubits used in the spectroscopy fits (including those of WTQ1 and WTQ7 whose data are not shown). The fits also allow us to extract the

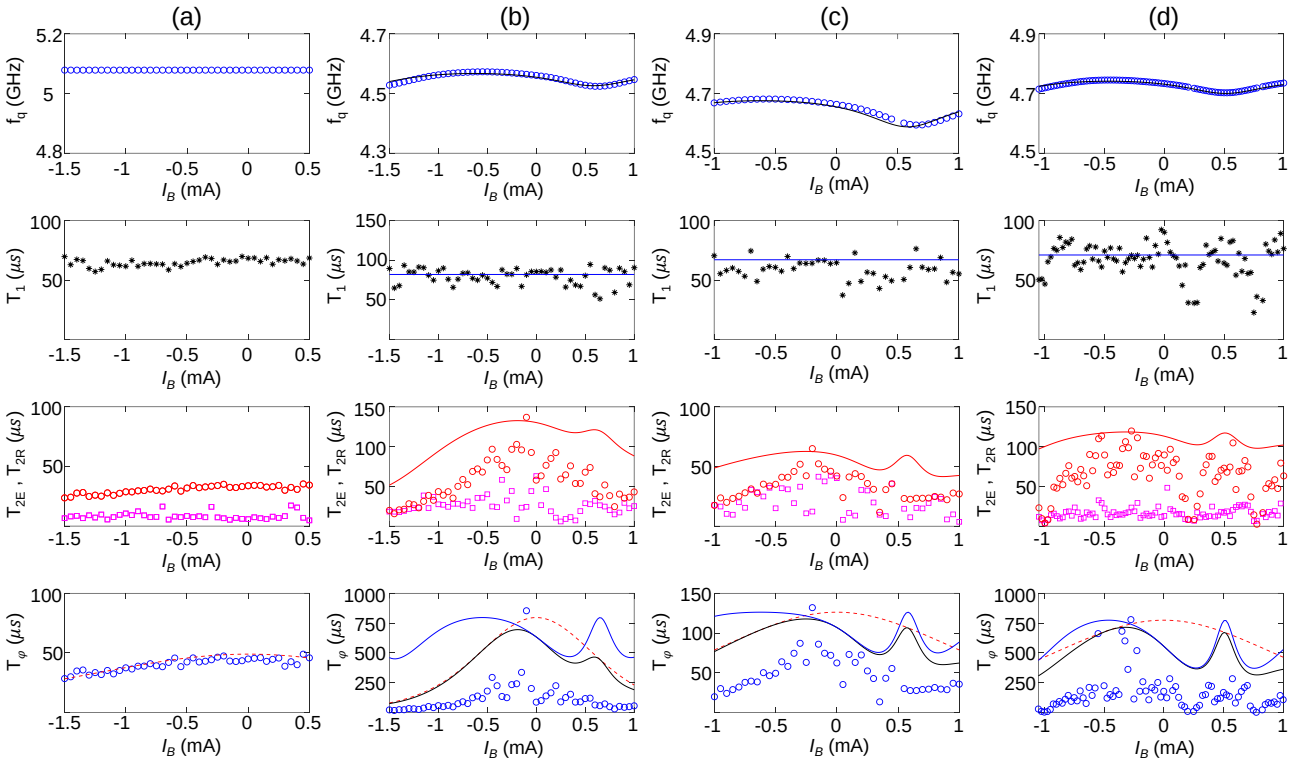


FIG. 9: Coherence measurements for chip A taken for Q4 (a), WTQ2 (b), WTQ3 (c), and WTQ5 (d). Top to bottom rows show the qubit frequency $f_{\rm q}$ (blue circles), T_1 (black stars), $T_{2\rm E}$, $T_{2\rm R}$ (red circles and magenta squares, respectively), and T_φ (blue circles) as a function of the applied coil bias current $I_{\rm B}$. The solid black curves in the first row plots represent theory fits for the qubit frequency based on the diagonalization of the Hamiltonian. The solid blue curves drawn in the second row plots, represent fits based on Eq. (74). The solid red curves shown in the third row plots correspond to the calculated $T_{2\rm E}$ based on the T_1 and T_φ fits (see main text). The dashed red, solid blue, and solid black curves shown in the fourth row plots represent the calculated $T_{\phi,\rm D}$, $T_{\varphi,\rm F}$, and T_φ fits, respectively (see main text and table V for details).

JJ asymmetry parameter of the dc-SQUIDs α_J for the various qubits, which we list in Tables I, II for chip A. As expected from the device physics, higher values of α_J correlate well with smaller observed δ of the WTQs.

As seen in the figure, the maximum and minimum qubit frequencies are obtained at $\Phi_x = 0$ and $\Phi_x = \pm\Phi_0/2$, respectively. The smallest δ of 50 MHz and 43 MHz are measured for WTQ2 and WTQ5, respectively, which are designed to have a slightly larger JJ asymmetry than WTQ3 and WTQ6, whose δ is 89 MHz and 86 MHz, respectively. Notably, the α_J extracted from the fits (see Table II), i.e., 3.5 and 2.8, match fairly well the dc resistance ratios measured for test JJs (fabricated on the same wafer) that have the same area ratios as the JJs of the SQUIDs.

Furthermore, using the spectroscopy data, we calculate the maximum and minimum magnitude of the WTQ anharmonicity given by $|\alpha| = |f_{12} - f_{01}|$ at the upper and bottom sweet spots corresponding to $\Phi_x = 0$ and $\Phi_x = \pm\Phi_0/2$, respectively (see Table I). For example, the anharmonicity of qubits with δ of $43-99$ MHz varies by $17-31$ MHz.

Similarly, Table III summarizes the main figures of merit measured for qubits in chip B, while Table IV lists the capacitance and critical current parameters of the various qubits in chip B extracted from their corresponding spectroscopy fits (not shown).

In Figs. 9, 10, we plot the measured coherence times for qubits in chip A and chip B respectively. In Fig. 9, the columns, from left to right, represent the results of the single-JJ transmon Q4 (a), WTQ2 (b), WTQ3 (c), and WTQ5 (d). The rows, from top to bottom, display the qubit frequency $f_{\rm q}$, relaxation time T_1, decoherence times $T_{2\rm E}$ (Echo) and $T_{2\rm R}$ (Ramsey), and extracted dephasing time given by $T_\varphi^{-1} = T_{2\rm E}^{-1} - (2T_1)^{-1}$, plotted as a function of I_B, i.e., the direct current applied to the global coil flux biasing the qubits.

The solid black curves in the first row plots represent theory fits based on the diagonalization of the WTQ Hamiltonian. The solid blue curves in the second row plots represent theory fits for T_1 calculated using Eq. (74). The upper bound of these fits is set to match the experimental data (typically T_1 that corresponds to the maximum $T_{2\rm E}$, listed in Table I (for chip A and Fig. 9)

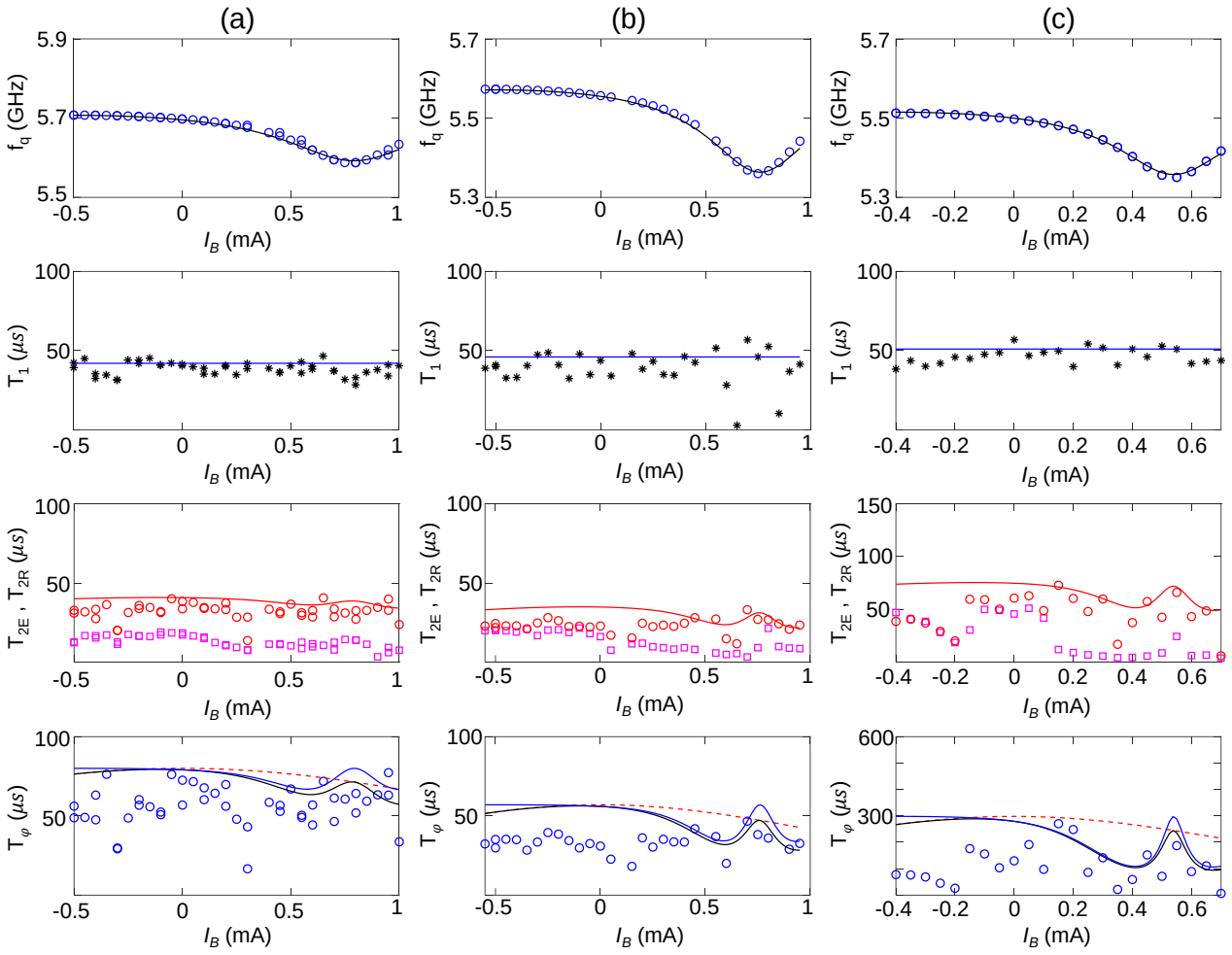


FIG. 10: Coherence measurements for chip B taken for WTQ2 (a), WTQ3 (b), and WTQ5 (c). Top to bottom rows show the qubit frequency $f_{\rm q}$ (blue circles), T_1 (black stars), $T_{2\rm E}$, $T_{2\rm R}$ (red circles and magenta squares, respectively), and T_φ (blue circles) as a function of the applied coil bias current $I_{\rm B}$. The solid black curves in the first row plots represent theory fits for the qubit frequency based on the diagonalization of the Hamiltonian. The solid blue curves drawn in the second row plots, represent fits based on Eq. (74). The solid red curves shown in the third row plots correspond to the calculated $T_{2\rm E}$ based on the T_1 and T_φ fits (see main text). The dashed red, solid blue, and solid black curves shown in the fourth row plots represent the calculated $T_{\phi,\rm D}$, $T_{\varphi,\rm F}$, and T_φ fits, respectively (see main text and table VI for details).

and Table III (for chip B and Fig. 10)). The average T_1 of the WTQs is similar to that of the fixed-frequency transmon Q4. This is consistent with the assumption that surface dielectric loss dominates relaxation in both the WTQ and the single-JJ transmon. Variations with flux as seen for instance in chip A, WTQ5 (Fig. 9)) also suggest frequency-dependent couplings to TLSes. However we did not explore this behavior systematically as was done in Ref. [22].

One important observation regarding the measured $T_{2\rm E}$ (red circles) and $T_{2\rm R}$ (magenta squares) plotted in the third row and T_φ (blue circles) drawn in the fourth row of Fig. 9, is that they exhibit a pronounced decrease with $|I_B|$, which strongly indicates that the decoherence times in our system are primarily limited by heating effects caused by large $|I_B|$. This observation is further supported by the fact that we observe a rise in the temperature of the mixing chamber stage by several milliKelvin during the lengthy data taking process of f_q, T_1, $T_{2\rm R}$, $T_{2\rm E}$ as I_B is swept (about 15 minutes for each I_B). Another supporting evidence of the heating effect we observe in our system, is the monotonic decrease in $T_{2\rm R}$, $T_{2\rm E}$, and T_φ of the single JJ-transmon (Q4) (see the first column plots), which to a large extent is insensitive to flux noise.

To model the dependence of the dephasing time on heating caused by $|I_B|$, we consider one of the dominant dephasing mechanisms in qubits that are dispersively coupled to readout resonators, which arise from fluctuation in the qubit frequency due to thermal photon

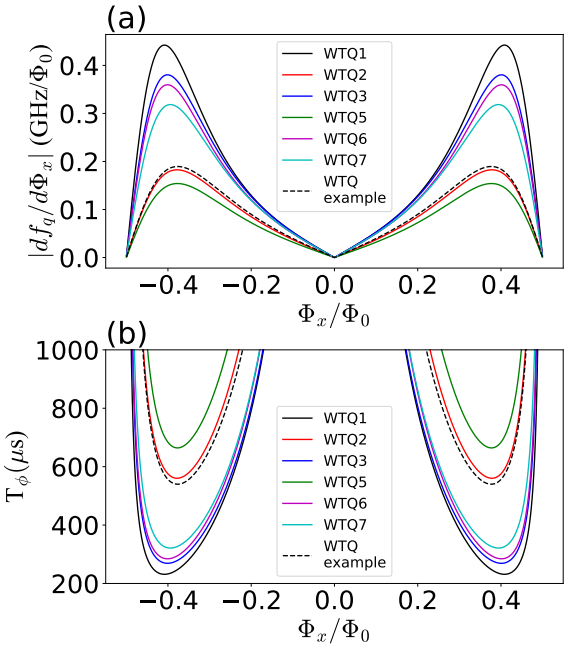


FIG. 11: (a) WTQ flux-sensitivities of qubits on chip A and of example device, found by numerical differentiation of Eq. (64), using device parameters listed in Table II and Fig. 5. (b) Flux-noise-limited dephasing times T_ϕ, assuming $1/f$ flux-noise amplitude $A_\Phi^{1/2} \sim 2\mu\Phi_0$ at 1 Hz.

population in the readout resonator [36]. In the limit $\bar{n} \ll 1$, the dephasing rate associated with this mechanism (denoted $\Gamma_{\phi,\mathrm{D}} \equiv T_{\phi,\mathrm{D}}^{-1}$) is given by [37]

$$\Gamma_{\phi,\mathrm{D}} = \Gamma_c \bar{n}, \tag{104}$$

where $\Gamma_c \equiv \kappa\chi^2/(\kappa^2+\chi^2)$, κ is the total photon decay rate of the fundamental mode of the readout resonator with angular frequency $\omega_r = 2\pi f_r$ (here κ is dominated by the coupling rate to the external feedline), χ is the qubit-state-dependent frequency shift of the readout resonator, and $\bar{n}$ is the average thermal photon number in the resonator, where $\bar{n} = 1/\left(e^{(\hbar\omega_r/k_B T_e)} - 1\right)$ is the Bose-Einstein population of the 50 Ohm external feedline (heat bath) at effective temperature T_e, which we express as $T_e = \bar{T}_e + \delta T$, where $\bar{T}_e$ is the effective temperature with no bias current ($I_B = 0$) and $\delta T = \Theta I_B^2$ represents the rise in the effective temperature of the device due to ohmic dissipation.

Note that δT can be expressed as $\delta T = C_H Q_d$, where C_H is the heat capacity of the device and $Q_d = R I_B^2 \tau_B/2$ is the dissipated heat energy in the flux biasing circuit, the experimentally relevant temperature-to-current conversion coefficient Θ can be expressed as $\Theta = RC_H\tau_B/2$, where τ_B is an effective measurement duration. In our qubit experiments, we find that Θ varies in the range $5-10$ mK/(mA)^2 for chip A (see Table V) and $3-7$ mK/(mA)^2 for chip B (see Table VI).

The dashed red curves in the fourth row plots of Fig. 9 represent the calculated $T_{\phi,\mathrm{D}}$ for Q4 (a), WTQ2 (b), WTQ3 (c), and WTQ5 (d). Similarly, the solid blue curves represent the calculated dephasing time $T_{\varphi,\mathrm{F}}$ that is set by the flux noise of the biasing circuit given by $T_{\varphi,\mathrm{F}}^{-1} = T_\phi^{-1} + T_{\phi,\mathrm{D}_0}^{-1}$, where T_ϕ is evaluated using Eq. (75) with $T = \bar{T}_m + \delta T$, where $\bar{T}_m$ is the effective temperature of the superconducting magnetic coil with no bias current, and T_{ϕ,D_0} is an experimental bound on dephasing time due to the dispersive coupling mechanism. It is worth noting that heating has a lesser effect on $T_{\varphi,\mathrm{F}}$ (solid blue curves) than $T_{\phi,\mathrm{D}}$ (dashed red curves). In the former case, heating causes the periodic response of T_ϕ to decrease with $|I_B|$. Likewise, the solid black curves, drawn in the forth row plots, represent the total dephasing time calculated using the relation $T_\varphi^{-1} = T_\phi^{-1} + T_{\phi,\mathrm{D}}^{-1}$, which accounts for the contribution of both dephasing mechanisms discussed above and exhibits a fair agreement with the data.

Finally, we plot a bound on $T_{2\mathrm{E}}$, drawn as solid red curves in the third row plots of Fig. 9, using the calculated T_φ and the relation $T_{2\mathrm{E}}^{-1} = (2T_1)^{-1} + T_\varphi^{-1}$.

In a similar manner, in Fig. 10 we plot using the same symbols and conventions of Fig. 9 tunability curves and coherence time measurements taken for qubits WTQ2 (a), WTQ3 (b), and WTQ5 (c) of chip B as a function of I_B and the corresponding theoretical fits.

VII. DISCUSSION

As seen in Figs. 9, 10, the WTQs exhibit coherence times, i.e., T_1 and T_φ, that are comparable to those of single-JJ transmons fabricated on the same chip. These times are consistent with the loss and dephasing mechanisms typically seen in single-junction transmons, i.e., surface dielectric loss [38] and dispersive coupling in the case of T_φ near the sweet spots (see the solid blue curves in the fourth row of Figs. 9, 10).

We attribute the larger than expected drop in the measured T_φ of the WTQs and transmons, observed for large $|I_B|$ (see blue circles), to the unintended heating side-effect produced by our flux biasing circuit as $|I_B|$ is varied. This undesired heating effect is extrinsic to the qubits and can in principle be mitigated by better thermal anchoring of the dc wires and the magnetic coil, reducing the parasitic resistance of the superconducting coils and the intermediate connectors carrying the dc current at the base-temperature stage, and realizing on-chip, superconducting flux lines with higher mutual inductance to the SQUID loops that directly flux-bias each qubit, thus requiring much smaller bias currents.

It is important to emphasize that the resistance of the flux biasing circuit affects the two dephasing mechanisms associated with our devices differently as reflected in the theoretical results of Fig. 6(a) and the experimental data in Figs. 9, 10. As seen in Fig. 6(a) a higher re-

sistance dampens the swings of the dephasing times at and away from the flux sweet spots, whereas higher resistance would increase the heating effect as seen in the experiment for large $|I_B|$. However, by applying some of the techniques outlined above, it should be possible to resolve this trade-off by reducing the heating effect in future systems.

While we do not observe flux-noise-limited dephasing in our experiment, we can estimate its effects. So-called 'universal' flux noise with an approximately $1/f$ power spectrum has been widely observed in superconducting systems. Its amplitude $A_\Phi^{1/2}$ at 1 Hz generally exceeds 1 $\mu\Phi_0$. [39, 40]. Following [19], we can write an approximate Ramsey dephasing rate $\Gamma_{\phi,R} = |df_q/d\Phi_x| \cdot 2\pi\sqrt{A_\Phi |\ln(2\pi f_{\rm IR} t)|}$, where $f_{\rm IR}$ is a cutoff frequency of 1 Hz, and t being on the order of $1/\Gamma_{\phi,R}$ we take to be 10 μs. We can find the flux sensitivity $|df_q/d\Phi_x|$ as a function of flux by differentiating Eq. (64) with respect to flux. For example, for the qubits on chip A, we can use circuit parameters in Table II and differentiate numerically in terms of fractional flux quantum, with units of GHz/Φ_0, as shown in figure 11 (a). If we conservatively assume $A_\Phi^{1/2} \sim 2\mu\Phi_0$, and taking the echoed dephasing rate $\Gamma_{\phi,E}$ according to [41] to be $\Gamma_{\phi,E} \sim \frac{1}{4}\Gamma_{\phi,R}$, and neglecting the contribution of qubit relaxation, we can estimate a lower bound for flux-noise-limited dephasing time $T_\phi \sim 1/\Gamma_{\phi,E}$. These dephasing times, shown in figure 11 (b) compare favorably to $T_2^e = 200$ μs which is projected to be the minimum necessary to achieve fidelity $\geq 99.9\%$ in cross-resonance gates [42]. The minimum dephasing times are comparable to the best average transmon dephasing times demonstrated in multi-qubit devices [43]. Using the example parameters of Fig. 5 we find a minimum flux-noise-limited dephasing time comparable to the dephasing times presented in Figs. 5 and 6.

It is worth noting that we do not observe an obvious advantage for either the P or U WTQ designs with respect to the measured relaxation time T_1 of the various qubits in both chips (or at least not in the range $50-100$ μs measured in the experiment).

It is also worth noting that, like single-JJ transmons, it is possible to adjust the maximum frequency of WTQs using focused laser beams following fabrication and JJ resistance measurement at room temperature [14]. This useful technique is applicable to WTQs because (1) the maximum frequency of WTQs is strongly dependent on the critical current of the non-SQUID JJ, (2) the non-SQUID JJ of WTQs is physically well separated from the SQUID in both designs, thus it may be annealed without considerably affecting the SQUID JJs. Such capability further enhances the ability of WTQs to avoid frequency collisions in large quantum systems as laser annealing can be selectively applied to WTQs across the chip (whose resistances are far off from their designed values), followed by, as necessary, an *in situ* fine-tuning using applied flux when the device is cold. Hence, selective laser-anneal, combined with in-situ flux tuning of WTQs, suggests a new avenue to reliably evade frequency collisions in large lattices of qubits, while maintaining high coherence. To quantify the effect on frequency-crowding, we can adopt the simplified model [14] that a 'collision free' device of N qubits requires every qubit to lie within a 'window' $\pm\Delta f$ of its frequency set-point. For normally distributed scatter at frequency precision σ_f, the likelihood of this occurring is found as the cumulative distribution function of $\Delta f/\sigma_f$, raised to the power N. For the conditions described in [14], a heavy-hexagon-type lattice of $N = 1000$ qubits has $\Delta f = 26$ MHz. WTQ tunability δ however in practice enlarges this 'window' by $\delta/2$. Taking the precision $\sigma_f = 18$ MHz shown for multi-qubit lattices in [15], we estimate that a 1000-qubit lattice made of WTQs of tunability $\delta = 50$ MHz can be made collision-free 10% of the time, while using WTQs of tunability $\delta = 99$ MHz gives a collision-free yield of 99%.

Following this work, there are several promising threads to pursue, such as: (1) Investigating the dependence of higher modes of the WTQ on applied flux, in particular the f_{10} mode that is theoretically calculated for the WTQ example of Fig. 5(c). (2) Demonstrating cross-resonance gates in multi-qubit chips of WTQs and showing that most frequency collisions can be avoided by applying independent fluxes to neighboring qubits. (3) Finding out the limits on the tunability ranges that can be experimentally achieved with these qubits. (4) Interrogating TLS spectra in the frequency and time domains by flux-tuning a WTQ.

VIII. CONCLUSION

We introduce weakly tunable superconducting qubits whose frequency can be tuned with external magnetic flux. The qubits comprise capacitively shunted JJ and asymmetric dc-SQUID, sharing one electrode and capacitively coupled via the other two.

We develop a theoretical model that captures the device physics and its coupling to the flux biasing circuit. By solving the full Hamilitonian of the system, we calculate the various qubit properties as a function of the circuit parameters and applied flux. We also calculate the qubit relaxation and dephasing times associated with the flux-biasing circuit. Furthermore, we derive analytical expressions that yield approximate values for the various device parameters and coherence times.

Moreover, we fabricate and test two superconducting chips containing several variations of these qubits. We show that they can achieve frequency tunablity ranges as low as $43-287$ MHz with only a small asymmetry in the size of their SQUID JJs ($\alpha_J = 2-3.5$), which are considerably lower than what is possible using highly-asymmetric dc-SQUID transmons (about 350 MHz of tunability with an asymmetry factor of 15). Using such weakly flux-tunable qubits should enable us to resolve most common frequency-collisions in multi-qubit architectures while minimizing sensitivity to flux noise. For example, a 1000-qubit device comprising WTQs of tun-

ability $\delta = 50$ MHz and trimmed using laser-anneal could achieve collision-free yield of 10% and dephasing times > 500 μs, while WTQs of tunability $\delta = 99$ MHz could achieve collision-free yield of 99% and dephasing times > 200 μs. Furthermore, in any large qubit lattice it is likely that several qubits will suffer degraded coherence due to TLS coupling. WTQ tunability can restore the qubits' T_1 and permit periodic adjustments if the TLSes drift over time [22].

These qubits also retain key properties of transmons, that make them quite useful in multi-qubit architectures, such as having $0-1$ transition frequencies in the range $4-5.5$ GHz, anharmonicities around $250-300$ MHz, comparable relaxation and decoherence times to single-JJ transmons, small footprints, and a standard fabrication process. Another important advantage of these qubits is that they couple together like transmons, therefore, likewise are expected to support cross-resonance gates and other two-qubit gates applicable to transmons in general.

Acknowledgments B.A., J.B.H. thank Malcolm Carroll, Easwar Magesan, and Jay Gambetta for fruitful discussions. B.A. highly appreciates Jim Rozen's help with wiring the dilution fridge. This work is partially funded by the IARPA Grant No. W911NF-16-1-0114-FE. Contribution of the U.S. Government, not subject to copyright.

[1] P. W. Shor, Polynomial-Time Algorithms for Prime Factorization and Discrete Logarithms on a Quantum Computer, SIAM J. Sci. Statist. Comput. **26**, 1484 (1997).
[2] N. Moll *et al.*, Quantum optimization using variational algorithms on near-term quantum devices, Quantum Sci. Technol. **3**, 030503 (2018).
[3] A. Kandala *et al.*, Hardware-efficient variational quantum eigensolver for small molecules and quantum magnets, Nature **549**, 242 (2017).
[4] A. W. Cross, L. S. Bishop, S. Sheldon, P. D. Nation, J. M. Gambetta, Validating quantum computers using randomized model circuits, Phys. Rev. A 100, 032328 (2019).
[5] A. G. Fowler, M. Mariantoni, J. M. Martinis, A. N. Cleland, Surface codes: Towards practical large-scale quantum computation, Phys. Rev. A **86**, 032324 (2012).
[6] E. Dennis, A. Kitaev, A. Landahl, J. Preskill, Topological quantum memory, J. Math. Phys. 43, 4452 (2002).
[7] J. Koch *et al.*, Charge-insensitive qubit design derived from the Cooper pair box, Phys. Rev. A **76**, 042319 (2007).
[8] H. Paik *et al.*, Observation of High Coherence in Josephson Junction Qubits Measured in a Three-Dimensional Circuit QED Architecture, Phys. Rev. lett. **107**, 240501 (2011).
[9] C. Rigetti *et al.*, Superconducting qubit in a waveguide cavity with a coherence time approaching 0.1 ms, Phys. Rev. B **86**, 100506(R) (2012).
[10] C. Rigetti and M. Devoret, Fully microwave-tunable universal gates in superconducting qubits with linear couplings and fixed transition frequencies, Phys. Rev. B **81**, 134507 (2010).
[11] J. M. Chow *et al.*, Simple All-Microwave Entangling Gate for Fixed-Frequency Superconducting Qubits, Phys. Rev. Lett. **107**, 080502 (2011).
[12] See peekskill system information on https://quantum-computing.ibm.com/
[13] S. Sheldon, E. Magesan, J. M. Chow, and J. M. Gambetta, Procedure for systematically tuning up cross-talk in the cross-resonance gate, Phys. Rev. A **93**, 060302(R) (2016).
[14] J. B. Hertzberg, E. J. Zhang, S. Rosenblatt, E. Magesan, J. A. Smolin, J.-Bang Yau, V. P. Adiga, M. Sandberg, M. Brink, J. M. Chow and J. S. Orcutt, Laser-annealing Josephson junctions for yielding scaled-up superconducting quantum processors, npj Quant. Info. 7, 129 (2021).
[15] E. Zhang *et al.*, High-fidelity superconducting quantum processors via laser-annealing of transmon qubits, arXiv:2012.08475.
[16] A. D. Córcoles *et al.*, Demonstration of a quantum error detection code using a square lattice of four superconducting qubits, Nat. Commun. **6**, 6979 (2015).
[17] M. Takita, A. D. Córcoles, E. Magesan, B. Abdo, M. Brink, A. Cross, J. M. Chow, and J. M. Gambetta, Demonstration of Weight-Four Parity Measurements in the Surface Code Architecture, Phys. Rev. Lett. **117**, 210505 (2016).
[18] A. Morvan, L. Chen, J. M. Larson, D. I. Santiago, and I. Siddiqi, Optimizing frequency allocation for fixed-frequency superconducting quantum processors, arXiv:2112.01634v1 (2021).
[19] M. D. Hutchings, J. B. Hertzberg, Y. Liu, N. T. Bronn, G. A. Keefe, M. Brink, J. M. Chow, and B. L. T. Plourde, Tunable Superconducting Qubits with Flux-Independent Coherence, PRApplied **8**, 044003 (2017).
[20] F. Yan *et al.*, The flux qubit revisited to enhance coherence and reproducibility, Nat. Commun. **7**, 12964 (2016).
[21] M. Bal *et al.*, Frequency trimming of superconducting fixed-frequency qubits, APS March Meeting 2019.
[22] M. Carroll, S. Rosenblatt, P. Jurcevic, I. Lauer, and A. Kandala, Dynamics of superconducting qubit relaxation times, arXiv:2105.15201 (2021).
[23] S. A. Caldwell *et al.*, Parametrically Activated Entangling Gates Using Transmon Qubits, Phys. Rev. Applied **10**, 034050 (2018).
[24] N. Didier, E. A. Sete, M. P. da Silva, and C. Rigetti, Analytical modeling of parametrically modulated transmon qubits, Phys. Rev. A **97**, 022330 (2018).
[25] J. M. Gambetta, A. A. Houck, and A. Blais, Superconducting Qubit with Purcell Protection and Tunable Coupling, Phys. Rev. lett. **106**, 030502 (2011).
[26] S. J. Srinivasan, A. J. Hoffman, J. M. Gambetta, and A. A. Houck, Tunable Coupling in Circuit Quantum Electrodynamics Using a Superconducting Charge Qubit with a V-Shaped Energy Level Diagram, Phys. Rev. Lett. **106**, 083601 (2011).
[27] S. A. J. Hoffman, S. J. Srinivasan, J. M. Gambetta, and A. A. Houck, Coherent control of a superconducting qubit with dynamically tunable qubit-cavity coupling, Phys. Rev. B **84**, 184515 (2011).

[28] G. Zhang, Y. Liu, J. J. Raftery, and A. A. Houck, Suppression of photon shot noise dephasing in a tunable coupling superconducting qubit, npj Quantum Information **3**, 1 (2017).

[29] G. Burkard, R. H. Koch, and D. P. DiVincenzo, Multilevel quantum description of decoherence in superconducting qubits, Phys. Rev. B **69**, 064503 (2004).

[30] D. P. DiVincenzo, F. Brito, and R. H. Koch, Decoherence rates in complex Josephson qubit circuits, Phys. Rev. B **74**, 014514 (2006).

[31] A. E. Ruehli, Inductance Calculations in a Complex Integrated Circuit Environment, IBM Journal of Research and Development **16**, Issue: 5 (1972).

[32] X. You, J. A. Sauls, and J. Koch, Circuit quantization in the presence of time-dependent external flux, Phys. Rev. B 99, 174512 (2019).

[33] R.-P. Riwar, D. P. DiVincenzo, Circuit quantization with time-dependent magnetic fields for realistic geometries, arXiv:2103.03577.

[34] F. Solgun and D. P. DiVincenzo, Multiport Impedance Quantization, Annals of Physics **361**, 605 (2015).

[35] F. Solgun, D. P. DiVincenzo and J. M. Gambetta, Simple Impedance Response Formulas for the Dispersive Interaction Rates in the Effective Hamiltonians of Low Anharmonicity Superconducting Qubits, IEEE Transactions on Microwave Theory and Techniques **67**, Issue: 3, (2019).

[36] A. A. Clerk and D. W. Utami, Using a qubit to measure photon-number statistics of a driven thermal oscillator, Phys. Rev. A **75**, 042302 (2007).

[37] Z. Wang *et al.*, Cavity Attenuators for Superconducting Qubits, Phys. Rev. Applied **11**, 014031 (2019).

[38] J. M. Gambetta *et al.*, Investigating Surface Loss Effects in Superconducting Transmon Qubits, IEEE Trans. on Applied Supercond., **27**, 1700205 (2017).

[39] F. C. Wellstood, C. Urbina, and J. Clarke, Low-frequency noise in dc superconducting quantum interference devices below 1K, Appl. Phys. Lett. **50**, 772 (1987).

[40] S. M. Anton *et al.*, Pure dephasing in flux qubits due to flux noise with spectral density scaling as $1/f^{\alpha}$, Phys. Rev. B **85**, 224505 (2012).

[41] J. Bylander *et al.*, Noise spectroscopy through dynamical decoupling with a superconducting flux qubit, Nat. Phys. **7**, 565 (2011).

[42] J. Ku *et al.*, Suppression of Unwanted ZZ Interactions in a Hybrid Two-Qubit System, Phys. Rev. Lett. **125**, 200504 (2020).

[43] E. Berg, Z. Minev, A. Kandala, and K. Temme, Probabilistic error cancellation with sparse Pauli-Lindblad models on noisy quantum processors, arXiv:2201.09866 (2022).

Qubit	α_J	$f_{01}^{\max}$ (GHz)	f_r (GHz)	$\lvert\alpha\rvert^{\max}$ (MHz)	$\lvert\alpha\rvert^{\min}$ (MHz)	δ (MHz)	T_1 (μs)	$T_{2E}^{\max}$ (μs)
WTQ1	2.6	4.8905	6.8869	254	224	99	75	85
WTQ2	3.5	4.57	6.9642	254	233	50	82	136
WTQ3	2.8	4.681	6.8372	246	215	89	64	65
Q4	NA	5.0785	6.9567	360	360	NA	65	36
WTQ5	3.5	4.442	6.9217	265	248	43	71	120
WTQ6	2.8	4.653	6.790	260	239	86	-	-
WTQ7	3.0	4.6065	6.867	252	226	76	-	-

TABLE I: Measured parameters of Chip A. Q4 is the single-JJ transmon on the chip. The SQUID JJ ratio parameter α_J is extracted from the spectroscopy fits. $f_{01}^{\max}$ is the maximum measured qubit frequency. $\alpha^{\max}$ ($\alpha^{\min}$) is the maximum (minimum) measured anharmonicity obtained at $f_{01}^{\max}$ ($f_{01}^{\min}$). δ is the measured frequency tunability range. $T_{2E}^{\max}$ is the maximum measured coherence and T_1 is the corresponding lifetime taken at the same flux bias. The coherence times for WTQ6 and WTQ7 were not measured.

Qubit	Design	α_S	C_1' (fF)	C_2' (fF)	C_c (fF)	I_{c1} (nA)	I_{c2} (nA)	I_{c3} (nA)	α_J (fit)
WTQ1	U	4.2	60.5	17.8	20.0	28.3	25.0	65.3	2.6
WTQ2	P	5.1	61	18.4	20.5	25.2	20.0	69.8	3.5
WTQ3	P	4.2	61	17.8	20.6	26.4	21.3	60	2.8
Q4	NA	NA	62.9	NA	NA	24.0	NA	NA	NA
WTQ5	U	5.1	60.0	18.4	20.0	23.4	20.2	70.7	3.5
WTQ6	U	4.2	60.7	18.3	20.1	25.9	21.3	60.0	2.8
WTQ7	P	4.2	60.0	18.1	20.7	25.4	20.0	60.2	3.0

TABLE II: Circuit parameters of chip A qubits extracted from the spectroscopy theory fits.

Qubit	α_J	$f_{01}^{\max}$ (GHz)	f_r (GHz)	$\lvert\alpha\rvert^{\max}$ (MHz)	$\lvert\alpha\rvert^{\min}$ (MHz)	δ (MHz)	T_1 (μs)	$T_{2E}^{\max}$ (μs)
WTQ2	2.36	5.6805	6.9683	252	224	115	42	40
WTQ3	2.06	5.557	6.8410	243	189	207	57	33
Q4	NA	6.375	6.967	349	349	NA	13	25
WTQ5	2.06	5.497	6.9262	250	161	159	47	73
WTQ6	1.9	5.743	6.7906	248	181	287	40	58
WTQ7	1.95	5.972	6.869	226	162	262	29	42

TABLE III: Measured parameters of Chip B. Q4 is a single-JJ transmon. WTQ1 did not yield (one of its SQUID junctions is open). The SQUID JJ ratio parameter α_J is extracted from the spectroscopy fits. $f_{01}^{\max}$ is the maximum measured qubit frequency. $\alpha^{\max}$ ($\alpha^{\min}$) is the maximum (minimum) measured anharmonicity obtained at $f_{01}^{\max}$ ($f_{01}^{\min}$). δ is the measured frequency tunability range. $T_{2E}^{\max}$ is the maximum measured coherence and T_1 is the corresponding lifetime taken at the same flux bias. The relatively low T_1 of Q4 is limited by the Purcell effect due to the proximity of f_{01} to the readout frequency.

Qubit	Design	α_S	C_1' (fF)	C_2' (fF)	C_c (fF)	I_{c1} (nA)	I_{c2} (nA)	I_{c3} (nA)	α_J (fit)
WTQ2	P	3	61.4	18.3	20.0	37.9	40.0	94.4	2.36
WTQ3	P	2.9	61.5	18.5	20.7	36.9	36.0	74	2.06
Q4	NA	NA	62.9	NA	NA	36.7	NA	NA	NA
WTQ5	U	3	61.4	18.0	20.0	35.7	40.0	82.4	2.06
WTQ6	U	2.9	60.3	18.3	20.0	38.5	38.0	72.0	1.9
WTQ7	P	2.9	60.1	18.0	20.7	42.0	41.0	80.0	1.95

TABLE IV: Circuit parameters of chip B qubits extracted from the spectroscopy theory fits. WTQ1 on chip B is not measured because one of its SQUID junctions did not yield (open).

Qubit	$\kappa/2\pi$ (MHz)	$\chi/2\pi$ (MHz)	$\bar{T}_e$ (mK)	Θ mK/(mA)^2	$\bar{T}_m$ (K)	R (mΩ)
WTQ2	0.45	0.47	47	10	0.2	1
WTQ3	0.65	0.39	67	7	0.2	1
Q4	0.82	0.51	78	5	0.2	1
WTQ5	0.65	0.26	55	5	0.2	1

TABLE V: Parameters of chip A qubits used in the coherence measurement theory fits shown in Fig. 9

Qubit	$\kappa/2\pi$ (MHz)	$\chi/2\pi$ (MHz)	$\bar{T}_e$ (mK)	Θ mK/(mA)^2	$\bar{T}_m$ (K)	R (mΩ)
WTQ2	0.6	0.4	74	3	0.1	2
WTQ3	0.5	0.63	70	5	0.1	2
WTQ5	0.65	0.39	58	7	0.05	2

TABLE VI: Parameters of chip B qubits used in the coherence measurement theory fits shown in Fig. 10